



NTSB Battery Nail Penetration Tests

Final Report for 787 Battery (Asset 445) Tested at 15°C, Grounded

J. Thomas Chapin, PhD
Pravinray D. Gandhi, PhD, PE
Paul W. Brazis, Jr., PhD
May 29, 2014





Final Report for 787 Battery (Asset 445) Tested at 15°C, Grounded

NOTICE

The issuance of this Report does not constitute an endorsement of any proposed amendment and in no way implies Listing, Classification, or other recognition by UL and does not authorize the use of UL Listing or Classification Marks or any other reference to Underwriters Laboratories Inc. on, or in connection with, the product.

UL LLC, its employees, and its agents shall not be responsible to anyone for the use or nonuse of the information contained in this Report, and shall not incur any obligation or liability for damages, including consequential damages, arising out of or in connection with the use of, or inability to use, the information contained in this Report.

Release Type	<input type="checkbox"/> Internal <input checked="" type="checkbox"/> External (Confidential) <input type="checkbox"/> External (Public)	
UL Distribution	UL Corporate Research and UL staff signed onto the Mutual Non-Disclosure Agreement with the NTSB.	
External Distribution	Release approved only to the National Transportation Safety Board (NTSB) – Release subject to Mutual Non-Disclosure Agreement (NDA).	
Date:	Keywords: NTSB, 787 battery, Li-ion battery, Nail penetration test, internal short-circuit.	
Title: NTSB Battery Tests - Final Report For 787 Battery (Asset 445) Tested At 15°C, Grounded		
Author(s)	Department	Email
Paul Brazis Pravinray D. Gandhi	Corporate Research	Paul.brazis@ul.com Pravinray.d.gandhi@ul.com
Reviewer(s)	Department	Email
J. Thomas Chapin	Corporate Research	j.thomas.chapin@ul.com



ACKNOWLEDGEMENTS

The authors would like to thank the following individuals for their significant contributions to this work:

Dana Schulze, Bob Swaim, Mike Bauer, Dave Helson, and Mike Hauf from the NTSB.

Simon Lie, Mehdi Barekatein, and Jim Russell from Boeing Inc.

The authors also would like to thank the following UL employees for their significant contributions to this work:

Paul Courtney

David Dubiel

Alvin Wu

Carl Wang

Laurie Florence

Dan Steppan

Lyle Wright



TABLE OF CONTENTS

Notice	2
Acknowledgements	3
Final Report for 787 Battery (Asset 445) Tested at 15°C, Grounded	6
Background	6
Battery Asset 445 Characterization and Preparation	6
Nail Penetration Test	7
UL Test Facility	7
Nail Penetration Battery Test Fixture	8
Instrumentation and Data Acquisition	10
Heat and Smoke Release Measurement System	10
Gas FTIR Analyzer	15
Videos and Photography	15
Battery and Cell Electrical and Thermal Measurement	15
Test Procedures.....	17
Results	18
Test Observations	18
Heat, Smoke, and Vent Effluent Analysis	19
Smoke Release Analysis.....	21
Gas Effluent Analysis	21
Electrical and Thermal Testing Data and Analysis.....	23
Post Test Disassembly	39
Appendix A – Post-Test Disassembly Photos.....	42
Post- Test Photos – Nail Penetration Apparatus and Intact Battery	42
Post Test Disassembly Photos – Intact Battery	42
Battery Post Test Disassembly Photos - Insulation Materials.....	43
Battery Post Test Disassembly Photos – Cell 1	50
Battery Post Test Disassembly Photos – Cell 2	52
Battery Post Test Disassembly Photos – Cell 3	54



Battery Post Test Disassembly Photos – Cell 4	55
Battery Post Test Disassembly Photos – Cell 5	56
Battery Post Test Disassembly Photos – Cell 6	57
Battery Post Test Disassembly Photos – Cell 7	65
Battery Post Test Disassembly Photos – Cell 8	66
Appendix B – Battery Pre-Test Disassembly Analysis	68
Internal Battery Disassembly	68
Bus Bar Observation	70
Equipment Documentation	70
OCV Measurement	71
Cell Observations	71
Equipment Documentation	72
Cell Dimension and Weight Measurement	72
Appendix C – Infrared Spectra from Asset 445 Nail Penetration Test	77



FINAL REPORT FOR 787 BATTERY (ASSET 445) TESTED AT 15°C, GROUNDED

Background

NTSB requested UL to conduct nail penetration tests on Boeing 787 batteries under controlled conditions. The batteries tested were of the original (“901”) design. NTSB specified that these tests be conducted under a controlled (indoor laboratory) environment and prescribed that the tests be conducted at 100% state-of-charge. There was a desire to investigate the effect of ungrounded versus grounded (through battery charger) batteries to determine the effect on failure behavior. UL provided additional measurements, including heat release, smoke release, and characterization of smoke emissions. Temperature and voltage measurements, as well as wideband frequency measurements were conducted during each test. Batteries were provided by Boeing by the request of NTSB, and witnessed by NTSB investigators, as well as a Boeing engineer. Details regarding the battery sample are provided in the next section.

Battery Asset 445 Characterization and Preparation

The battery test sample (Asset 445) was provided by Boeing at the request of NTSB and shipped to UL Taiwan for disassembly, analysis, and characterization. The following non-destructive tests were performed on battery Asset 445:

- Battery disassembly and measurements (torque, DC/AC resistance and open-circuit voltage (OCV) of cells in the case)
- Cell measurements (visual inspection, weight, dimensions, OCV, AC/DC resistance)
- Computed Tomography (CT)
- Replace #445 Cells 1 and 2 with #271 Cells 1 and 2¹
- Drill holes on the lid
- Attach thermocouples
- Reassemble battery

Details of the battery disassembly and pre-test characterization can be found in Appendix B of this report.

¹ Cells 1 and 2 from battery Asset 445 were damaged during disassembly, and therefore were replaced with identical cells from battery Asset 271. Non-destructive and nail penetration testing continued with replacement cells.



Nail Penetration Test

The nail penetration test was performed at UL's Northbrook facilities. The battery was equipped with additional test measurement leads as described later in the report.

UL Test Facility

The tests were conducted in UL's Cell A test facility. The test cell is a 35 x 35 x 40 ft. high test room equipped with a 14 x 14 ft. collection hood to collect fire effluents (smoke, and gases). The collection hood is connected to UL's smoke abatement system through a 24 in. exhaust duct. Incorporated in the exhaust duct, is an instrumented section for measurement of smoke density and gases from a fire. The smoke density is measured using a photometric system consisting of a white light source and a photo detector to measure the opacity of the smoke. Heat release rate is calculated using an oxygen consumption technique². To enable this, duct velocity is monitored using a bi-directional probe, and the exhaust gases are monitored using a paramagnetic oxygen analyzer. The heat release rate system in Cell A has a capacity to measure a maximum 2 MW fire size. A photograph of the Cell A is shown in Figure 1.



Figure 1. Cell A

² W. J. Parker, "Calculations of Heat Release Rate by Oxygen Consumption for Various Applications", U. S. Department of Commerce, National Bureau of Standards, Center for Fire Research, Washington DC, 20234, NBSIR 81-2427-1, (1982).

Nail Penetration Battery Test Fixture

A nail penetration test fixture was developed to enable controlled nail penetration of the test batteries. The set-up included a load frame with a fixture that contained a nail penetration ram. The ram was designed such that its downward direction was controlled using hydraulic fluid pressurized by compressed air; and upward direction was controlled by compressed air. A photograph of the nail penetration test set-up is shown in Figure 2.

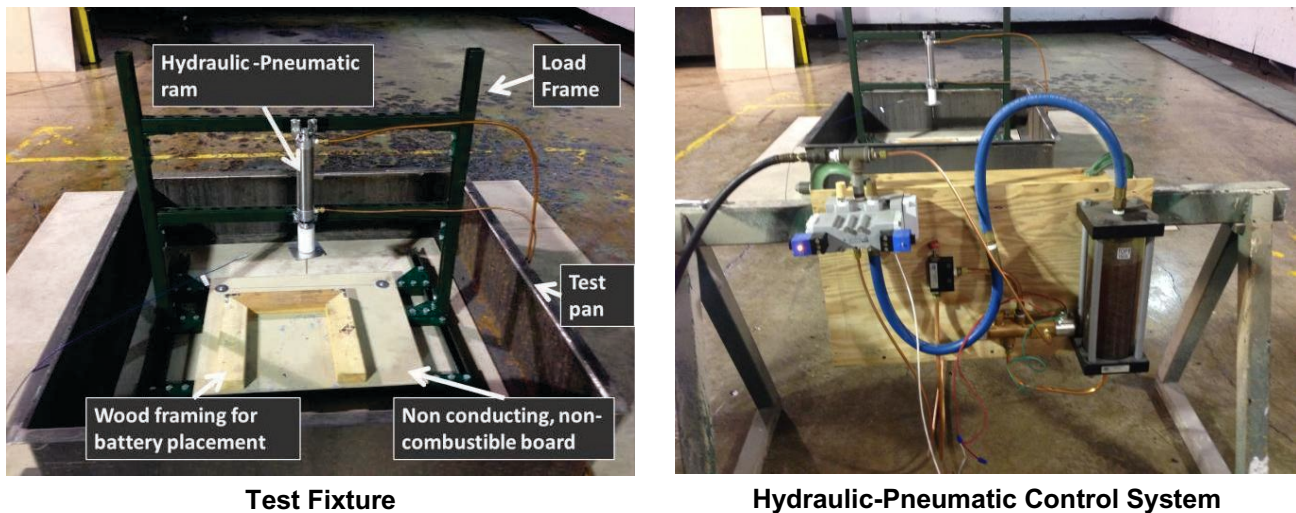


Figure 2. Nail Penetration Test Set-Up

A non-conducting and non-combustible board was placed at the bottom of the load frame, and a wood frame screwed into the board to allow precision placement of the test battery with respect to the nail.

A specially designed nail³ was used in the test. The nail is 126 mm long, with a diameter of 5 mm, and nail angle of 60°. A unique feature of the nail is an embedded thermocouple that provides temperature of the cell as it penetrates the battery. An annotated photograph of the nail is presented in Figure 3.

³ Type B, Number 1 nail from Yamamoto Technologies Company Limited, 4-7, Setoguchi 2-Chome, Hirano-Ku, Osaka 547-0034 Japan.

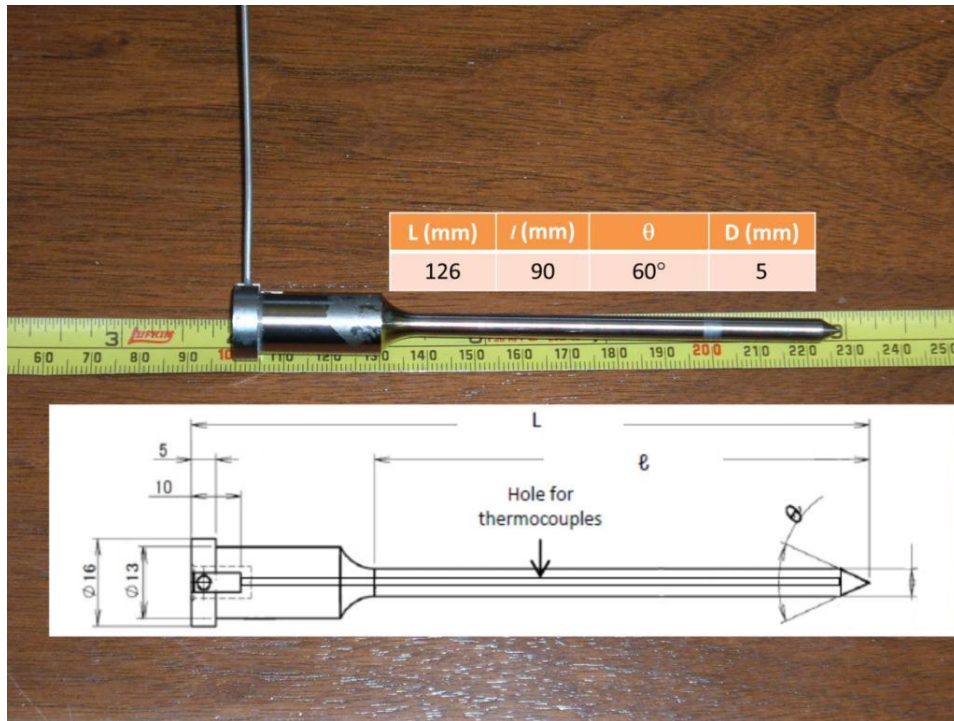


Figure 3. Test Nail

A close-up of the nail in the load frame is shown in Figure 4.



Figure 4. Test Nail in Load-frame

Instrumentation and Data Acquisition

Heat and Smoke Release Measurement System

The heat release rate is calculated using oxygen consumption technique. The system consists of a paramagnetic oxygen analyzer to measure the oxygen concentration; and bi-directional probe and thermocouple to measure the exhaust duct velocity. The smoke release rate is calculated using light transmission measurement consisting of a regulated light source, and a photoelectric detector. The measurement equipment used is described herein.

Oxygen Concentration Measurement

The oxygen analyzer was Siemens Oxymat 6 with a range from 0 to 25% oxygen.

Velocity Measurement

The velocity is measured using a bi-directional probe and a thermocouple. A schematic of the bi-directional probe is shown in Figure 5.

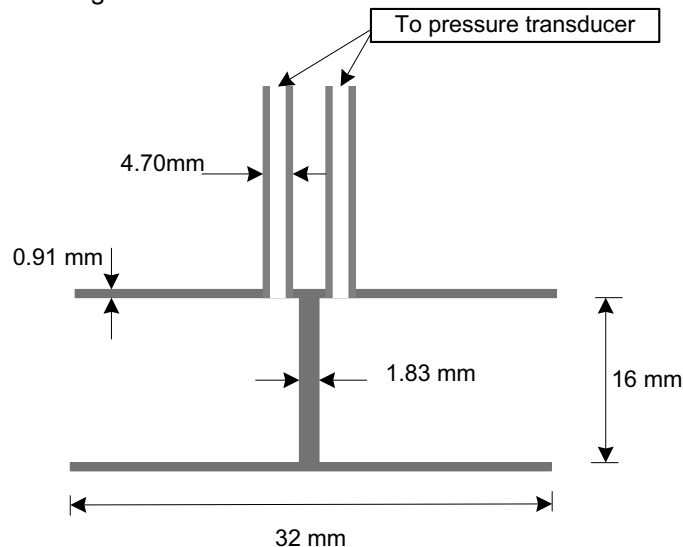


Figure 5. Bi-directional Probe

The bi-directional probe was connected a pressure transducer (MKS, Model: 220B) with a range of 0 – 10 mm Hg. The thermocouple used was 0.125 mm Inconel sheathed, Type K thermocouple.

The pressure and velocity data was used to calculate the flow velocity using Eq. 1.

$$V = C_v \sqrt{\Delta P \cdot T} \quad \text{Eq. 1}$$

where

- V is the velocity (m/s);
- C_v is the calibration constant for the bi-directional probe (= 0.806)
- ΔP is the pressure difference across the bi-directional probe (mm Hg); and
- T is flow temperature (K);

Smoke Density Measurement

The smoke optical density was measured using a white light source and a Photronic cell (Weston, Model: 856-9901013-BB). The optical density is calculated as a function of transmitted light using Eq. 2.

$$OD = \text{Log}_{10} \left(\frac{I_o}{I} \right) \quad \text{Eq. 2}$$

where

- OD is the optical density;
- I_o is the clear beam signal (V); and
- I is the test signal (V).

Calibration of Heat and Smoke Release Rate Measurements

The heat release rate system was calibrated using propane gas sand burner with known fire sizes of 75, and 200 kW; and a calibration factor was calculated. This range of the calibration fire sizes were selected based upon anticipated fire size during the test. The calibration for heat release rate is depicted in Figure 7. A calibration factor of 0.92 was applied to the calculation of heat release rate data during the test.

A photograph of the set-up used for heat release rate calibration is presented in Figure 6.



Figure 6 – Heat Release Rate Calibration Set-Up

The heat release rate is calculated using exhaust flow, and oxygen concentration data as shown in Eq. 3.

$$HRR = C_1 \cdot 17.15 \times 10^3 \cdot A \cdot V \cdot \left(\frac{298}{T} \right) \left(\frac{0.2095 - O_2}{\alpha - \beta O_2} \right) \quad \text{Eq. 3}$$

where

- C_1 is calibration factor (equal to 0.92)
- 17.15×10^3 is energy release per volume of oxygen consumed at 298 K (kJ/m³)
- A is duct area (m², equals 0.2919 for Cell A system)
- V is exhaust flow velocity (m/s)
- T is exhaust flow temperature (K)
- O_2 is oxygen concentration
- α constant for propane gas (equals 1.084)
- β constant for propane gas (equals 1.4)

The smoke measurement system was calibrated using neutral density filters. The calibration for the smoke measurement system is shown in Figure 8. A correction factor of 0.98 was applied to the calculated optical density data from the test.

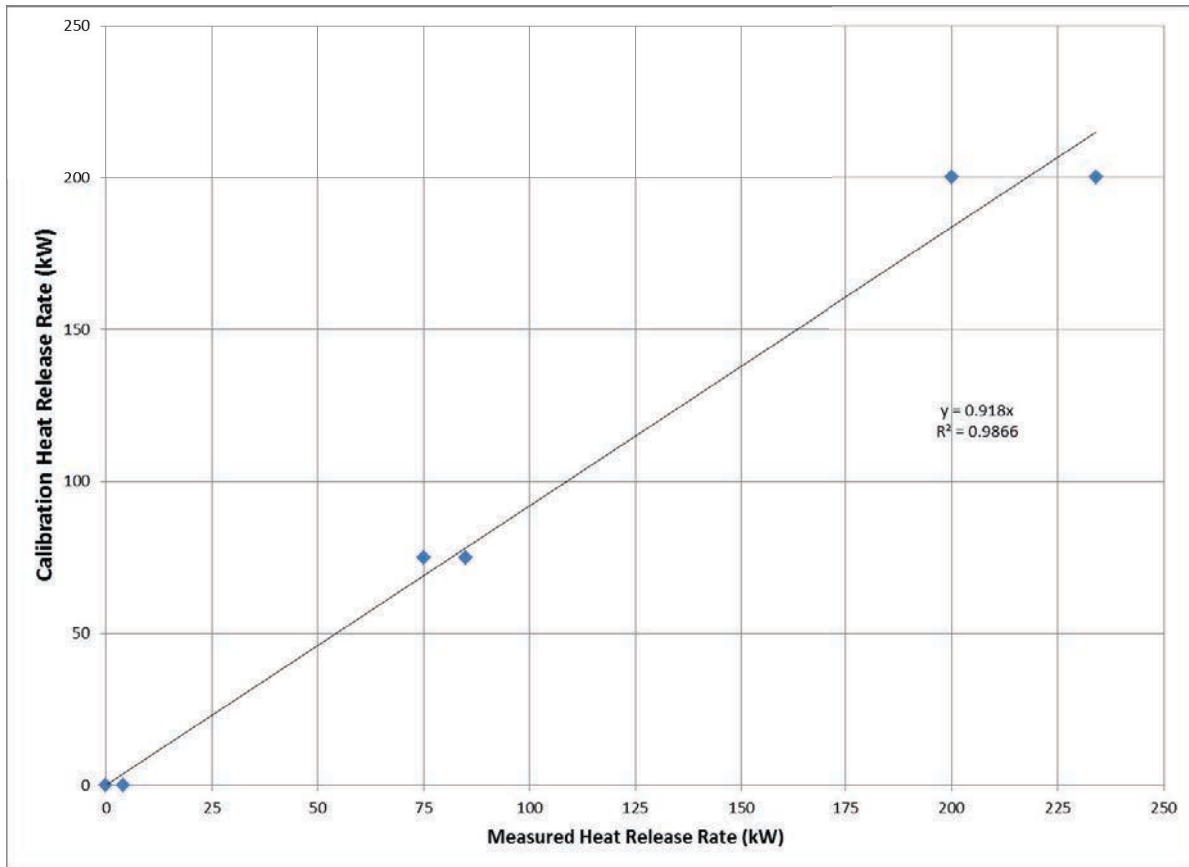


Figure 7. Heat release rate calibration

The smoke measurement system was calibrated using reference neutral density filters and the transmitted light output was used to calculate optical density as shown in Eq. 4.

$$OD = \text{Log}_{10} \left(\frac{I_o}{I} \right) \quad \text{Eq. 4}$$

where

- OD is the calculated optical density
- I_o is the clear beam signal (volts)
- I is the transmitted light signal (volts)

A calibration constant was then developed by correlating the calculated optical density with the neutral density filters as shown in Figure 8.

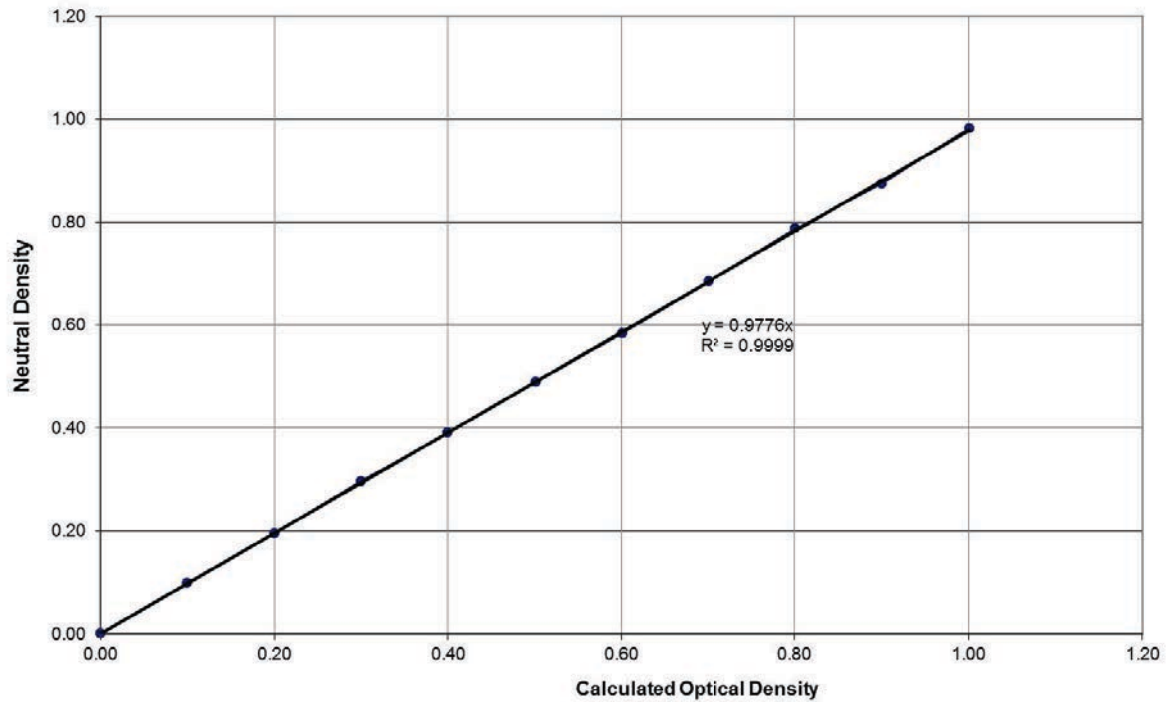


Figure 8. Smoke obscuration system calibration.

Smoke release rate is calculated using optical density and duct velocity data as shown in Eq. 5.

$$SRR = C_2 \frac{V \cdot A}{L} \text{Log}_{10} \left(\frac{I_o}{I} \right) \quad \text{Eq. 5}$$

where:

- C_2 is the optical density calibration factor (=0.98)
- SRR is smoke release rate (m^2/s)
- V is exhaust flow velocity (m/s)
- A is duct area (m^2 , equals 0.2919 for Cell A system)
- L is the path length (m , equals 0.6096 m for Cell A system)
- I_o is the clear beam signal (volts)
- I is the signal during the test (volts)



Gas FTIR Analyzer

A heated gas sampling probe, connected to a gas FTIR analyzer, was added to the instrumented duct section to extract the gases vented from the test battery during the test. The gas FTIR analyzer has a resolution of 0.5 cm^{-1} , and a path length of 10 m and can measure gas signatures in the range from $650 - 4500\text{ cm}^{-1}$. The FTIR analyzer continuously extracted gases from the instrumented duct at a rate of 4.2 L/min. The analyzer developed an average of 4 scans and provided an overall gas sampling rate of approximately 10 samples per minutes.

Videos and Photography

Digital video and still photography was used to document the tests. A total of five video cameras, and two Infra-red cameras were used to capture the fire tests from different angles. Three digital still photography cameras were used to capture key events during the tests.

Battery and Cell Electrical and Thermal Measurement

Figure 9 shows a photograph of the voltage and temperature cabling installed within the 15°C battery. The thermocouples used for temperature measurement, were Omega Nextel® Ceramic-Braided Type K thermocouples, XC Series. These thermocouples were 24 AWG and shielded with a ceramic-braided material for increased thermal resistance, rated for continuous use at 1200°C. Sixteen of these Type K thermocouples were added to the top surface (Face 5) of each battery cell, located on the busbars nearest each cell terminal. To optimize the thermal interconnection, the junction was attached directly under voltage sensing screws that are included as a part of the battery construction. For both thermocouple types, locations for each thermocouple are detailed for each cell discussion in the data analysis section.

Voltage leads were attached at nine electrical nodes in order to monitor the voltage across each of the eight cells. Three additional voltage leads were added to monitor the voltage at the grounding connector on the battery box, the voltage on the case of Cell 6, and the voltage at the positive terminal on the main battery power connector. Ground and battery voltages were referenced to the negative terminal of the battery (connected to the negative terminal of Cell 1). These voltage leads were constructed using insulated oven wire, Type MG, nickel-plated copper, shielded with fiberglass insulation over mica tape. This cable is specified for operation at 840°F, selected to maximize operational lifetime for the test.

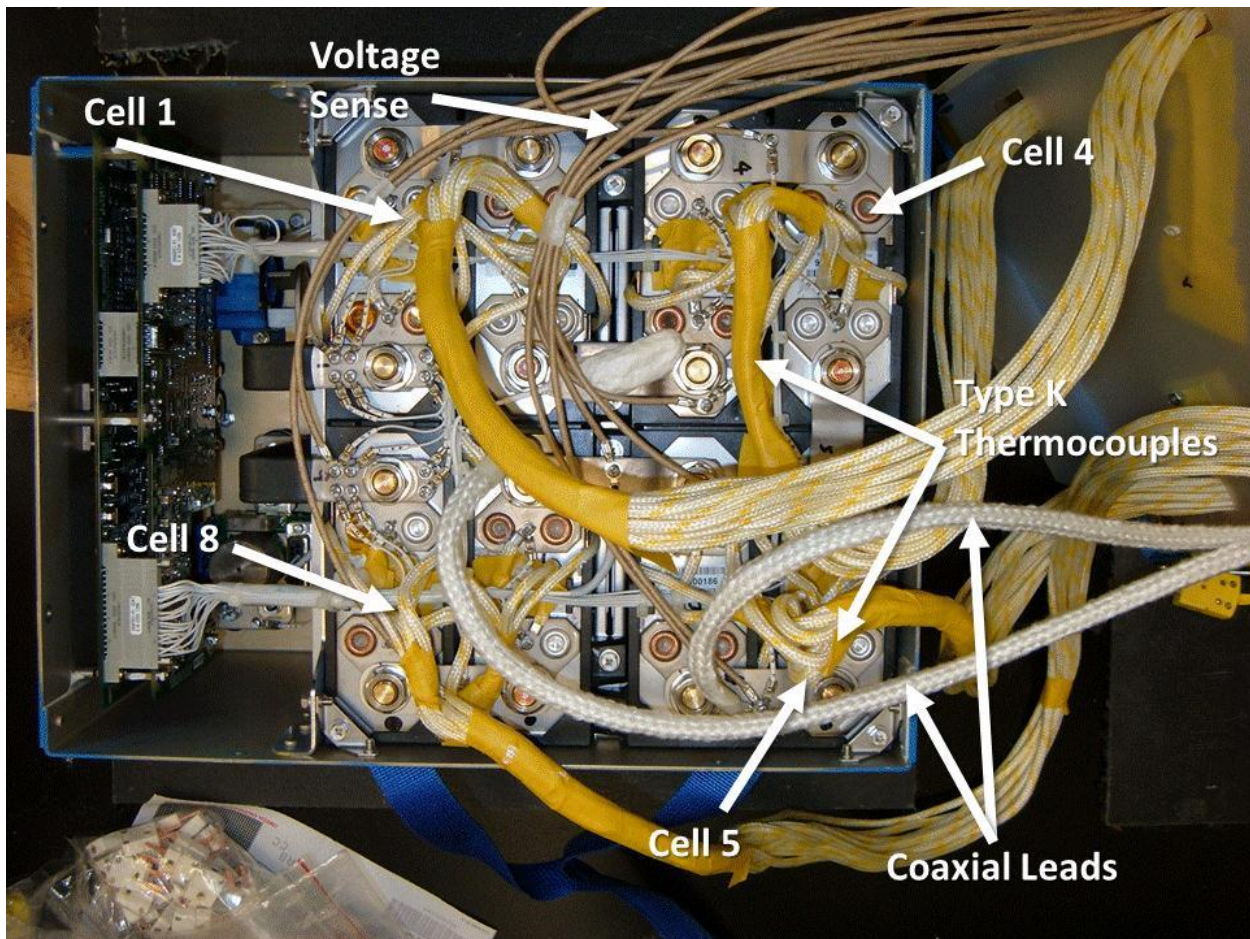


Figure 9. Photo of voltage and temperature sensing wiring for 15°C battery.

Voltage leads were made by crimping ring terminals to each of the voltage leads, and then attached using the existing screw terminals. The case connection to Cell 6 was made through compression of a bare voltage sense lead between the metal case of Cell 6 and the black plastic frame holding Cell 6 into the battery assembly. This interconnect was verified using a handheld multimeter and mechanically checked for integrity after installation.

The voltage and temperature leads were connected to two Agilent Model 34970A Data Acquisition Switch Units, which enabled scanning and recording of the data. Thermocouple and voltage leads were interfaced to these units using six Agilent Model 34901A relay cards. These units were then connected via GPIB interface to a laptop computer for data acquisition. Data for all voltage, current, and temperature channels were recorded in CSV format, approximately every 2-3 seconds.



A battery charging/monitoring unit (BMU) was connected to the battery. This was activated and provided an electrical grounding path between the negative terminal of the battery, the battery case, and the negative terminal of the BMU. Ground current was measured using a 1000A current shunt connected to the 12 AWG grounding wire [REDACTED] using 8 AWG cabling. This ground interconnect was then connected to the negative/ground terminal of the battery charging unit. Current flow on the ground wire was then monitored by measuring the voltage drop across the current shunt. The positive terminal of the battery was connected to the positive terminal of the BMU. Power was provided to the BMU through an external DC power source. The BMU and power supply were left on throughout the entire test, and control signals from the BMU were recorded during the duration of the test. A 10A load was available for loading of the battery, but was not used until at the end of the test to discharge the cells which did not vent during the test.

Coaxial cables were attached to each of the two terminals of Cell 6 in order to measure spectral noise. These coaxial cables were stripped of their outer insulation and shield to a distance of 18 inches from the cable end to minimize potential shorting of the coaxial ground to live parts in the battery during test. Interconnects were made using a crimped ring terminal that was then attached to existing screw terminals across Cell 6. The coaxial cable was thermally shielded using ¼ inch glass braid from the interconnect point out to a minimum of 12 inches after exiting the battery case. The coaxial cable was then connected to a high-speed digitizer card (National Instruments Model PXI-5922) via a differential probe. The differential signal across Cell 6 was recorded repeatedly, each for a duration of 100 ms. Due to instrument limitations, continuous recording was not attainable. Over the course of the entire test, 1999 samples of 100 ms each were recorded. These were then processed using LabVIEW-based automated software to calculate FFT spectra and record maximum, minimum, and average magnitude at each frequency point over the 1999 spectral files.

Test Procedures

For both the batteries, the following test procedures were used.

1. Remove the battery from the conditioning chamber
2. Connect the battery sensors (e.g., voltage, thermocouples) to data acquisition system
3. Place the battery in the nail penetration test fixture and connect all sensors to the data acquisition system
4. Conduct safety review
5. Verify all instrumentation, video and photographic documentation are working
6. Start 1 minute countdown
7. Initiate test by energizing the piston to penetrate the battery
8. Continue data collection until directed by NTSB staff to stop.



Results

Test Observations

During the test, photographs were taken to document the venting of the battery after nail penetration. These are presented in the series on photographs below.

Test Photos – reference NPT initiation 2:39

Nail penetration event reference 10:04

Cell 6 photo) event (approximated 90 seconds after nail penetration started)

Ref G0010486 10:06



Cell 6 photo) event (approximated 2 minutes after nail penetration started)

Ref G0010487 10:06



Heat, Smoke, and Vent Effluent Analysis

Heat release, smoke release, and gases were analyzed from the venting battery. *While the battery vented, there were no observations of flaming external to the battery.*

The heat release rate was calculated using oxygen consumption technique and Eq. 1.

The heat release rate is calculated using exhaust flow, and oxygen concentration data as shown in Eq. 6.

$$HRR = C_1 \cdot 17.15 \times 10^3 \cdot A \cdot V \cdot \left(\frac{298}{T} \right) \left(\frac{0.2095 - O_2}{\alpha - \beta O_2} \right) \quad \text{Eq. 6}$$

where

- C_1 is calibration factor (equal to 0.92)



- 17.15×10^3 is energy release per volume of oxygen consumed at 298 K (kJ/m^3)
- A is duct area (m^2 , equals 0.2919 for Cell A system)
- V is exhaust flow velocity (m/s)
- T is exhaust flow temperature (K)
- O_2 is oxygen concentration
- α constant for testing with complex chemistries (equals 1.105)
- β constant for testing with complex chemistries (equals 1.5)

The heat release rate for the test is shown in Figure 10. There was one vent event in Test 2; and the calculated heat release rates were relatively small, and are below the resolution of the Cell A heat release calorimeter.

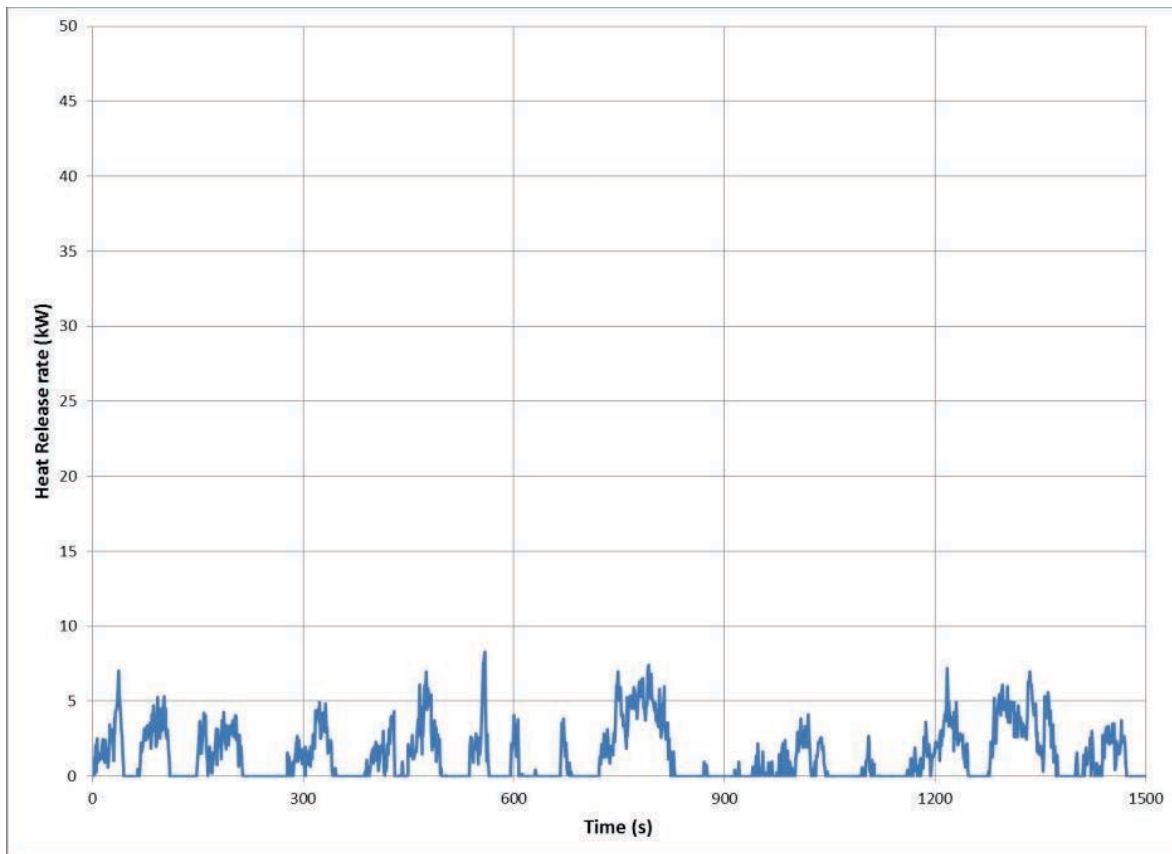


Figure 10. Heat release rate for the 15°C test.



Smoke Release Analysis

Smoke release rate is calculated using optical density and duct velocity data as shown in Eq. 5. The smoke release rate data are presented in Figure 11. The data shows distinct release of gases after the Cell 6 was shorted with nail penetration procedure. In this test, only Cell 6 vented.

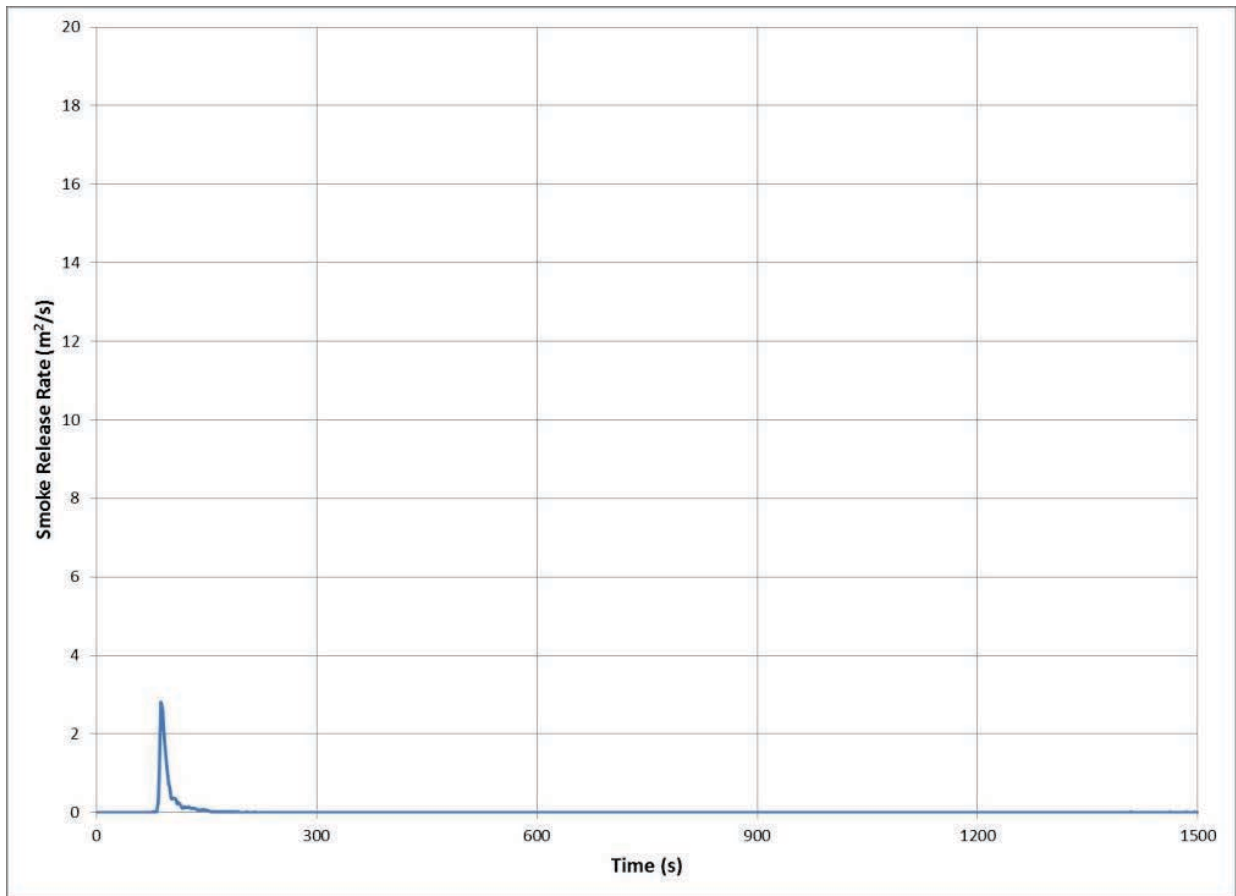


Figure 11. Smoke release rate from the 15°C test.

Gas Effluent Analysis

Gas effluent analysis is a specific method to define gas species by using FTIR technique. Aldrich vapor phase sample library, EPA vapor library, and UL in house library were used to identify the species in the effluent. The smoke release rate figure was tagged to enable linking the gases released to specific vent events as shown in Figure 12. There was only one vent event in this test.

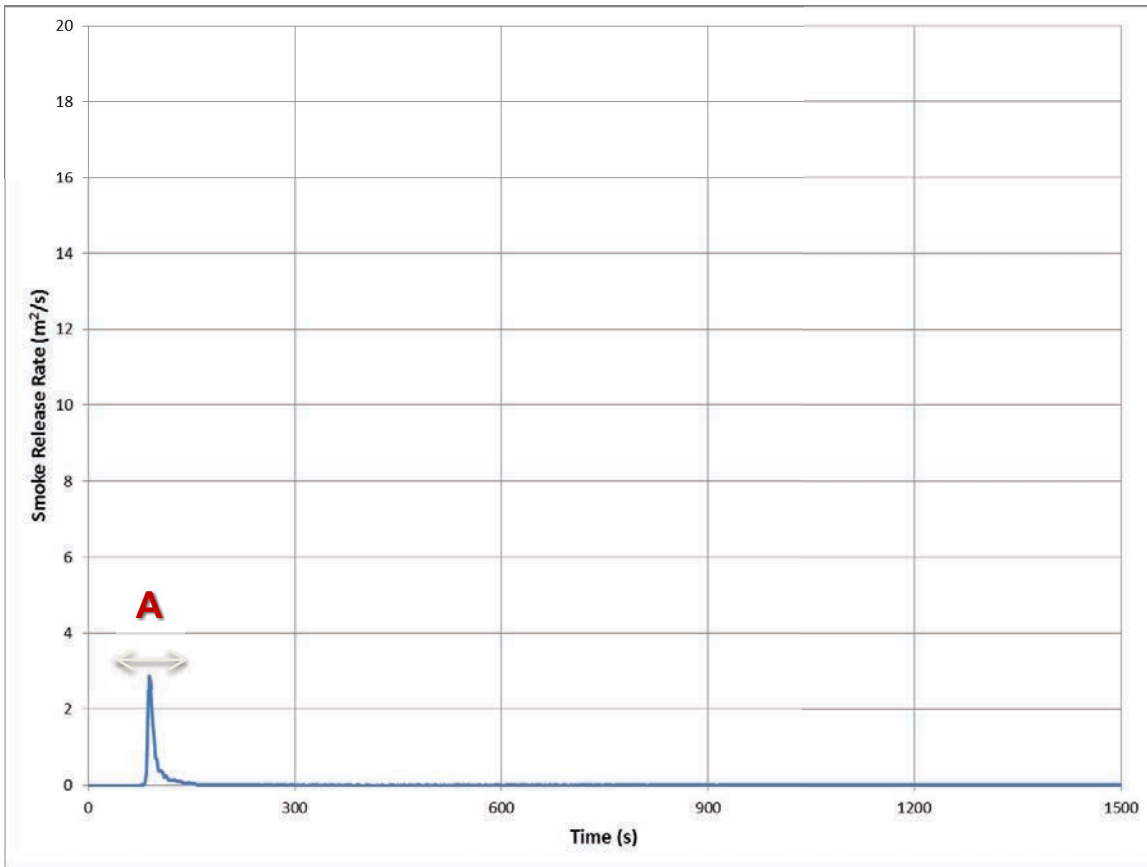


Figure 12 – Vent Event Identified for Gas Analysis

The gas effluent analysis results correlated to the Smoke Release Rate data were shown in Table 1. In the venting period (Zone A), the species in the vented smoke include the solvents in electrolyte, small hydrocarbons, CO, CO₂, and water.

Table 1. Gas Analysis for Vent Event

Zone	Gas Species	Time Duration *	Peak High *	Remark
A	DMC, EMC, CO ₂ , H ₂ O, CH ₄ , CO, C ₂ H ₄ , C ₂ H ₂	09:55:55' ~ 10:00:09'	09:56:48' ~ 09:57:16'	Please see Appendix C for IR spectra

DMC = Dimethyl carbonate; EMC =Elthymethyl carbonate; CO = Carbon monoxide.

*This test was conducted on 14 March 2014.



Electrical and Thermal Testing Data and Analysis

Initial Cell Voltages

The battery was fully charged prior to temperature conditioning and testing. Table 2 shows the voltages of each cell prior to start of the nail penetration test.

Table 2. Cell voltages at start of test.

Cell	1	2	3	4	5	6	7	8
Voltage (V)	4.00568	4.00973	4.00672	4.00265	4.00906	4.00973	4.01462	4.00717

The only cell to vent was Cell 6, the cell that was penetrated by the nail. The following sections show the temperatures measured at each battery.

Cell 6

Nail penetration into Cell 6 occurred at between 57 and 60 seconds after the start of the test. This was characterized by shorting of the Cell 6 case to the cell positive terminal, likely through the conductive nail. Temperature rise within the battery began to occur no less than two seconds after the penetration event. This rise coincides with the first drop in cell voltage, likely due to the failure and internal shorting of one of the three sub-cells. This causes a rise in temperature observed at the faces. Once this internal short clears, cell voltage returns to 4V and the rate of heating decreases. Temperature rise resumes once the other cells fail and cell voltage drops towards zero.

As with the prior test, the nail temperature (and therefore the battery interior) was at a higher temperature than that at the faces of the battery. As is seen in Figure 13, Face 1 exhibited the most temperature rise, particularly in relation to Face 2 (where the venting hole was located). As can be seen in Figure 14, temperature rise at Faces 2 and 3 continues for 400-500 seconds after nail penetration, and then commences a cool down for the remainder of the test. While significant heating was observed on the positive terminal of Cell 6 (thermocouple 6501), far less heating was observed on the negative terminal (thermocouple 6502). The reason for this is not clear, though it is possible that the thermal path was far more established to the positive side of the battery and the cell case, reflected in the Cell 6 case voltage rising to 4V and following the positive terminal voltage. This suggests electrical, and therefore, thermal shorting between the positive terminal, the cell interior, and cell case.

The voltage and current data show that the case of Cell 6 shorts to the battery case 92 seconds into the test (approximately 30 seconds after nail penetration). Current on the case ground wire was measured to be approximately 150 mA after nail penetration but prior to the shorting event, peaking at 629A at the



moment of the short formation. This shorting event lasted less than 3 seconds and fused open the 12 AWG ground wire, reducing the ground current to zero. After opening of the ground wire, the battery case was biased at 20V (referenced to the negative terminal of the battery) for the remainder of the test. The heating profile of Face 1 (thermocouple 6101) suggests that this short to the case was formed at Face 1 of Cell 6, as the temperature at Face 1 dropped at the instant of the high-current event, and then returned to a rapid temperature rise after opening of the ground wire. This suggests thermal transfer from Face 1 to the case at the moment of the establishment of metal-metal contact. The rate of heating observed at the nail also increased after the formation of the short to the case, which would reflect internal cell heating due to the flow of high current from Cell 6. The voltage rise to 20V suggests that the short was between the negative terminal of Cell 6, connecting the total voltage potential of Cells 1 through 5 to the battery case (referenced to the negative terminal of the battery, which is connected to the negative terminal of Cell 1). The Cell 6 case voltage showed a momentary increase to 6.5V then a drop to zero. This suggests that a momentary resistive path occurred through the interior of Cell 6 connecting the (initially shorted) positive terminal and the case of Cell 6 through a resistive path to the ground fault and therefore raising the potential of the case of Cell 6 towards 8V (the voltage across Cells 7 and 8). Once the ground fault cleared, this circuit either became highly resistive or opened, breaking the electrical connection between the case of Cell 6 and the positive terminal of Cell 6 (and therefore electrical connection to Cells 7 and 8).

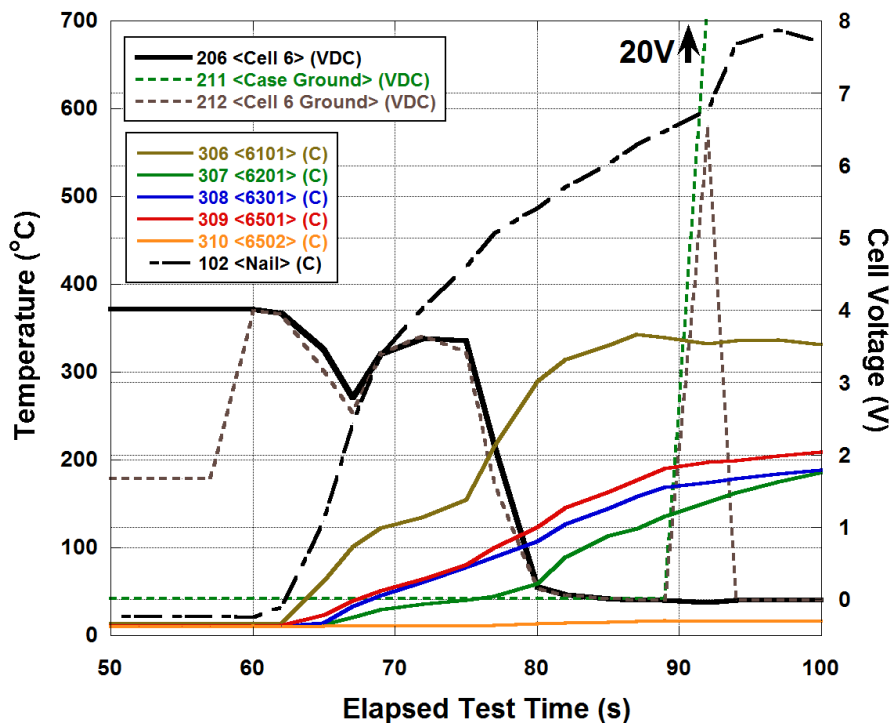


Figure 13. Voltage and temperature data for Cell 6 in the vicinity of the nail penetration event.

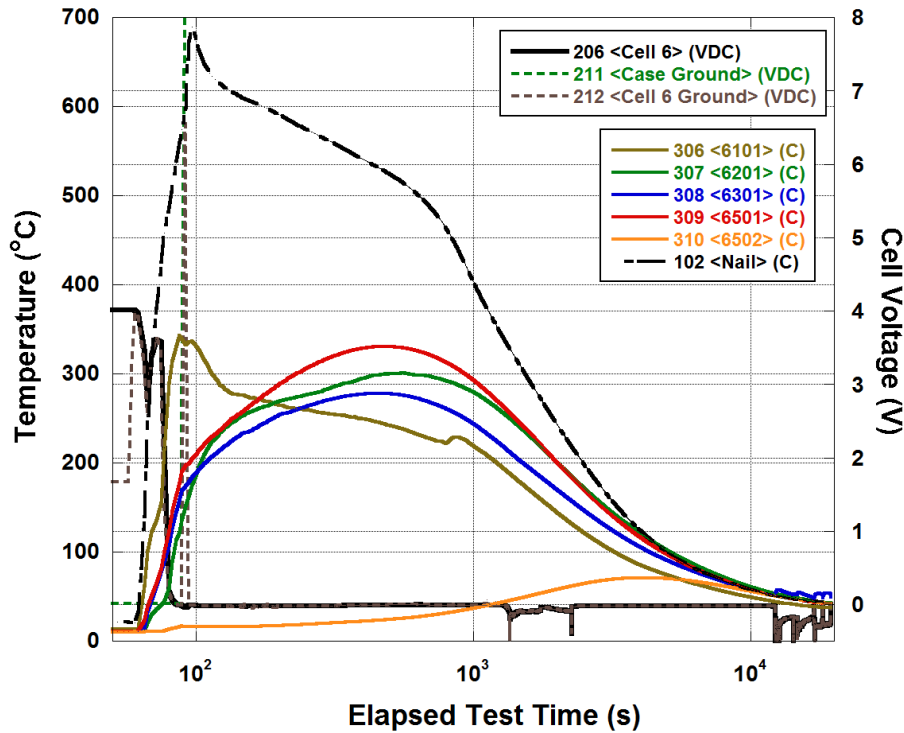


Figure 14. Voltage and temperature data for Cell 6, shown over the entire test duration.

Cells 5 and 7

Cells 5 and 7 were the only other cells to be exposed to temperatures above 70°C after venting of Cell 6. The most significant temperature rise was observed on the busbar between Cells 5 and 6, particularly in comparison to the measured temperatures on the other busbars connected to Cells 5 and 7. Most notably, the busbar connected between Cells 6 and 7 remained far cooler (by nearly 150°C) than the one between Cells 5 and 6. Considering also that Cell 5, and not Cell 7, showed a significant voltage drop during the shorting event, it is concluded that the short was located at (and biased to) the negative terminal of Cell 6, likely through the case of Cell 6 to the battery case. This placed a low-resistance short across Cells 1-5 (since the negative terminal of Cell 1 is connected to system ground), causing high current drain until the 12 AWG ground wire blew open. Once the current path blew open, the battery frame remained shorted to the negative terminal of Cell 6, biasing the case at 20V (the voltage across Cells 1-5). This high current flow then resulted in additional heating on the busbars between Cells 1-5. The busbar between Cells 5 and 6 received additional thermal energy from the venting event of Cell 6, rising the temperature of this busbar higher than the others. Since voltage was observed across the entire battery at the end of the test, it appears that the positive terminal of Cell 6 remained in electrical contact



with the rest of the circuit, though likely through a resistance consisting of the carbonized interior of Cell 6. During the shorting event it appears that Cells 7 and 8 were sufficiently electrically isolated from the shorting path to prevent loading of these cells during the event.

Thermal energy from the venting of Cell 6 was transferred to Cells 5 and 7 through their respective Faces 1 and 3, which were physically adjacent to Cell 6. Temperature rise was observed to roughly 1000 seconds, then reverting to cooling as thermal energy was transferred to Cells 1-4, as well as to the surrounding environment. The highest temperature on the faces of Cell 7 was observed on Cell 2, possibly due to exposure of hot escaping gases during the venting of Cell 6. This suggests that the gases escaped towards Cell 8 rather than towards Cell 5. However, since thermocouple 8201 (located on Face 2 of Cell 8) was not operating during the test, it is not possible to trace whether Cell 8 also received thermal energy from the flow of hot gases from Cell 6.

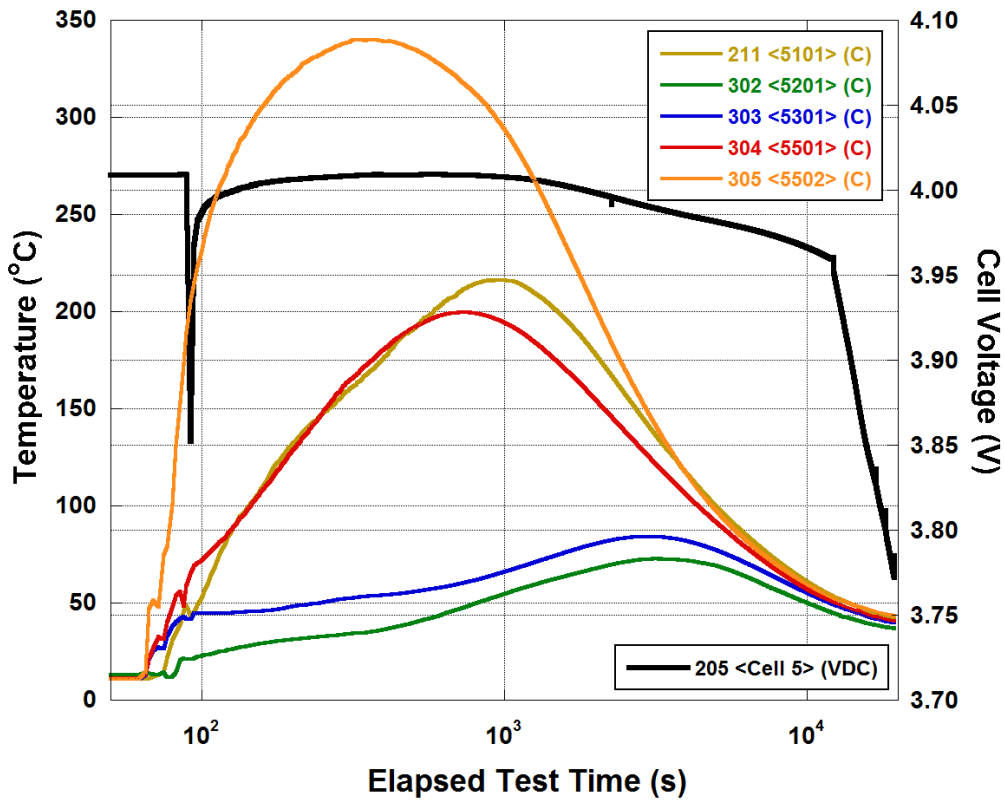


Figure 15. Voltage and temperature data for Cell 5 shown over the entire test duration.

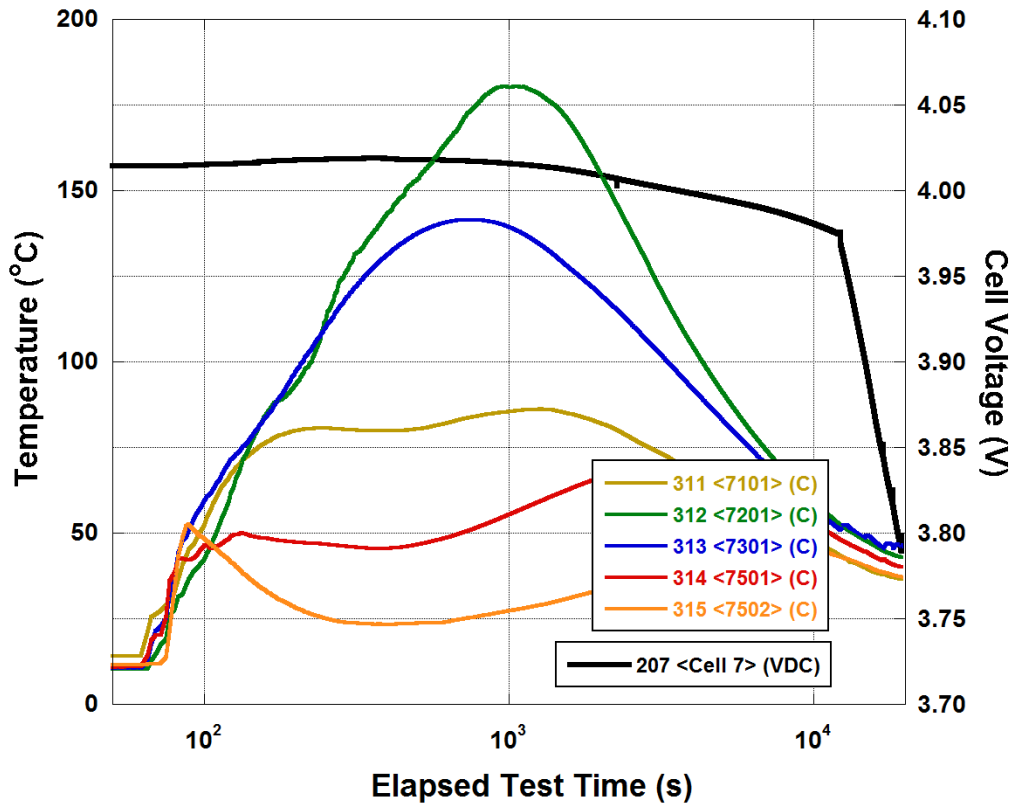


Figure 16. Voltage and temperature data for Cell 7 shown over the entire test duration.

Cells 1 Through 4

Cells 1 through 4 remained below 70°C throughout the entire test and did not vent. The most significant heating was observed during the shorting of Cell 6 case to the battery case, where the busbars of each cell increased in temperature. This was most likely due to Joule heating from the high current flow from the battery cells to the shorting event. This is followed by longer-term cooling, which reverses beyond 1000 seconds when excess heat from Cells 5-8 begins to transfer to Cells 1-4. The battery then begins to reach thermal equilibrium around 10000 seconds into the test and begins losing heat to the surrounding environment. No further events are observed in Cells 1-4.

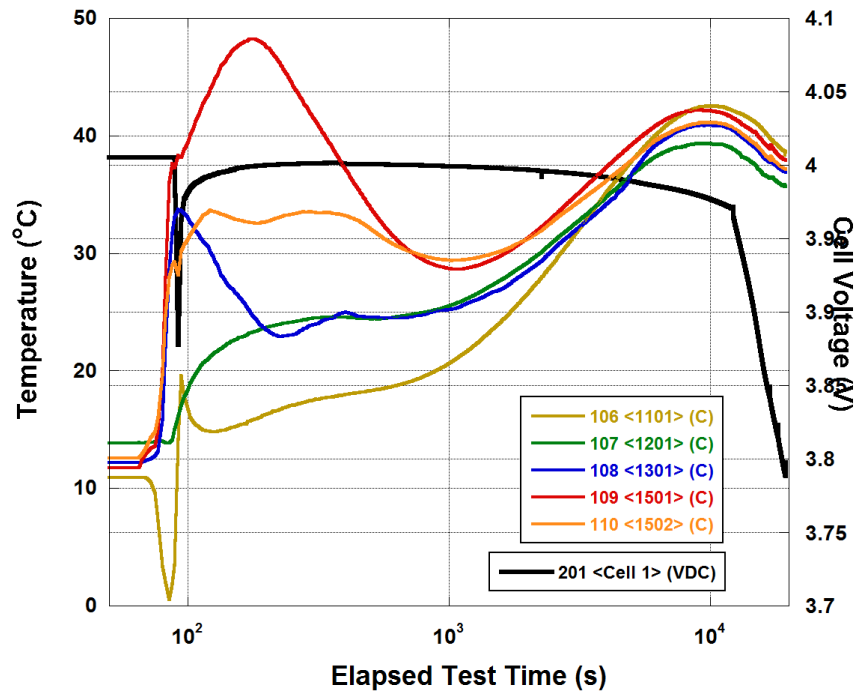


Figure 17. Voltage and temperature data for Cell 1 shown over the entire test duration.

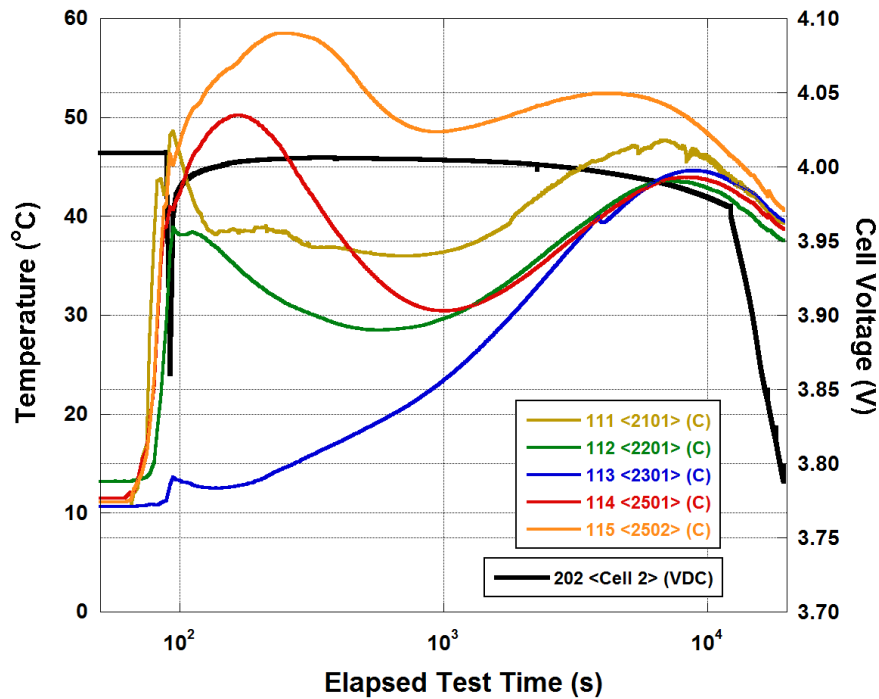


Figure 18. Voltage and temperature data for Cell 2, shown over the entire test duration.

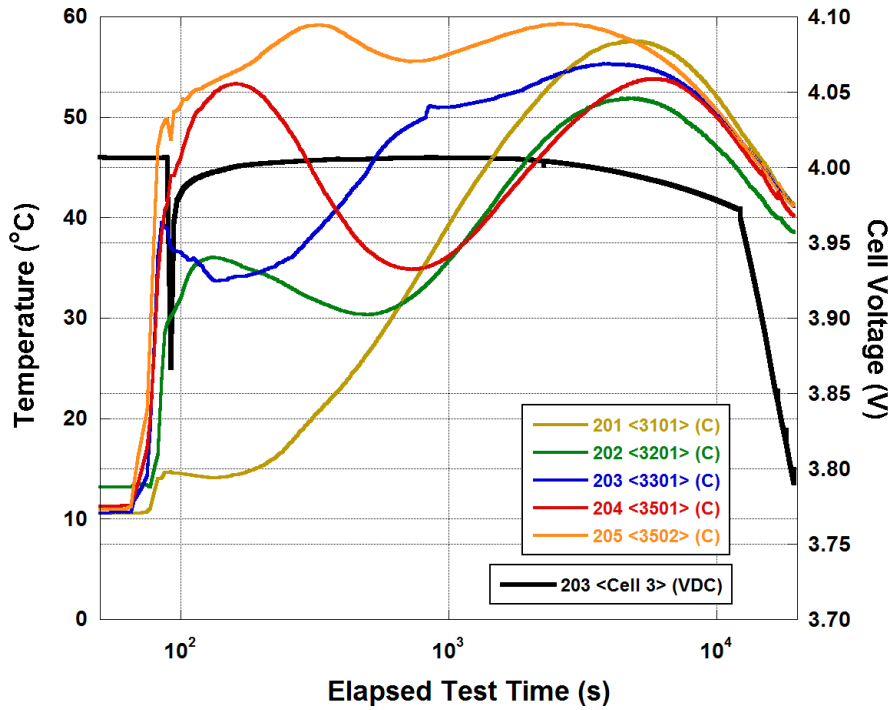


Figure 19. Voltage and temperature data for Cell 3 shown over the entire test duration.

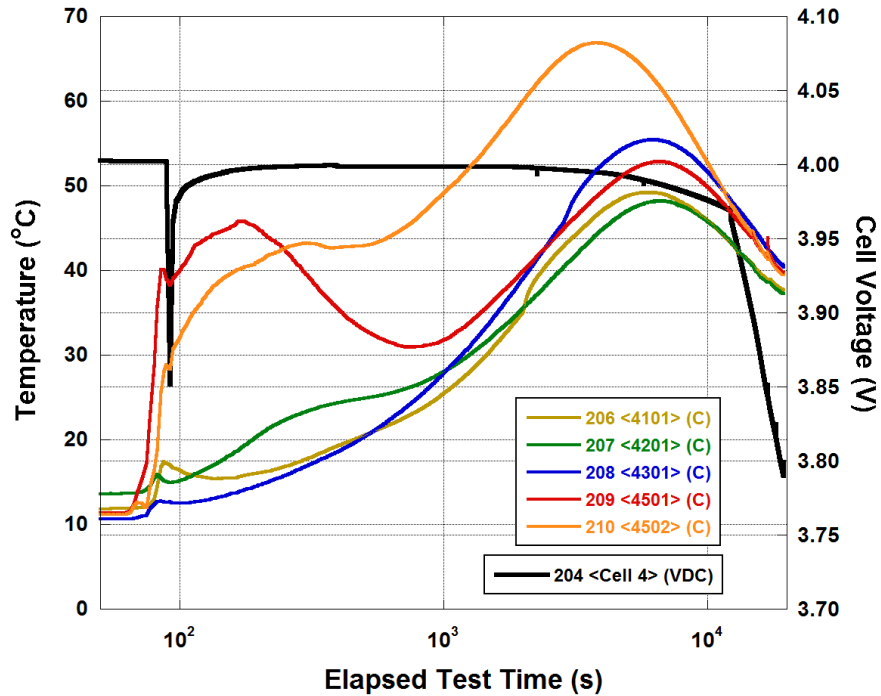


Figure 20. Voltage and temperature data for Cell 4 shown over the entire test duration.



Cell 8

The thermal data for Cell 8 (Figure 21) was similar to that as Cells 1-4, except for the absence of the busbar heating during the shorting event. This further supports the conclusion that the short within Cell 6 was between the negative terminal of Cell 6 and the battery case and an open circuit at the positive terminal, which resulted in no change in potential external to Cells 7 and 8, and therefore insignificant current flow from those cells since no other load was placed on Cells 7 and 8 (the positive terminal of Cell 8 was floating during the test). Heating therefore was only after 400-500 seconds into the test when the entire battery moved towards thermal equilibrium. Throughout the entire test, Cell 8 remained below 60°C.

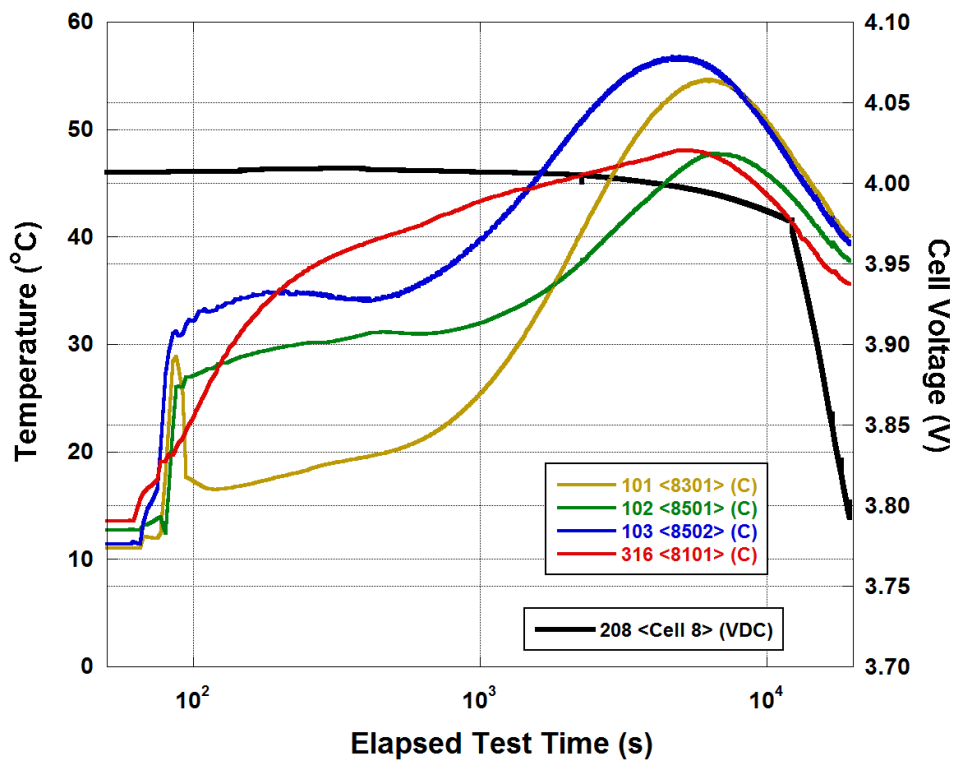


Figure 21. Voltage and temperature data for Cell 8 shown over the entire test duration.

Spectral Analysis

Through the duration of the test, 1,999 files of 100 ms each were recorded every 3.36 seconds, capturing the time-domain voltage across Cell 6. The voltage was sampled at 10 MS/s (10^7 samples per second, or 1 million samples over 100 ms), each sample with a resolution of 18 bits. These files were then



processed using automated LabVIEW-based software to calculate two FFT spectra, using 50,000 points for each spectrum.

One of the spectra was generated by first filtering the raw waveform through a digital low-pass filter (10-order Butterworth filter with -3 dB point at 250 kHz). This is then decimated by a factor of 20 to a 50,000-point waveform (decimating done by averaging each group of 20 datapoints to generate a single, averaged datapoint for the decimated file). The waveform is then passed through a Hanning window and the FFT is calculated. The resulting spectrum gives 10 Hz resolution to a maximum value of 250 kHz.

The second spectrum is generated by breaking the 100 ms waveform into twenty segments of 5 ms each. Each of these segments is passed through a Hanning filter and the FFT is calculated for each. These twenty spectra are then averaged together to give an average spectrum for the twenty segments. This method reduces the effect of random noise and preserves resolution at the highest frequencies. Resulting spectra have 200 Hz resolution to a maximum frequency of 5 MHz.

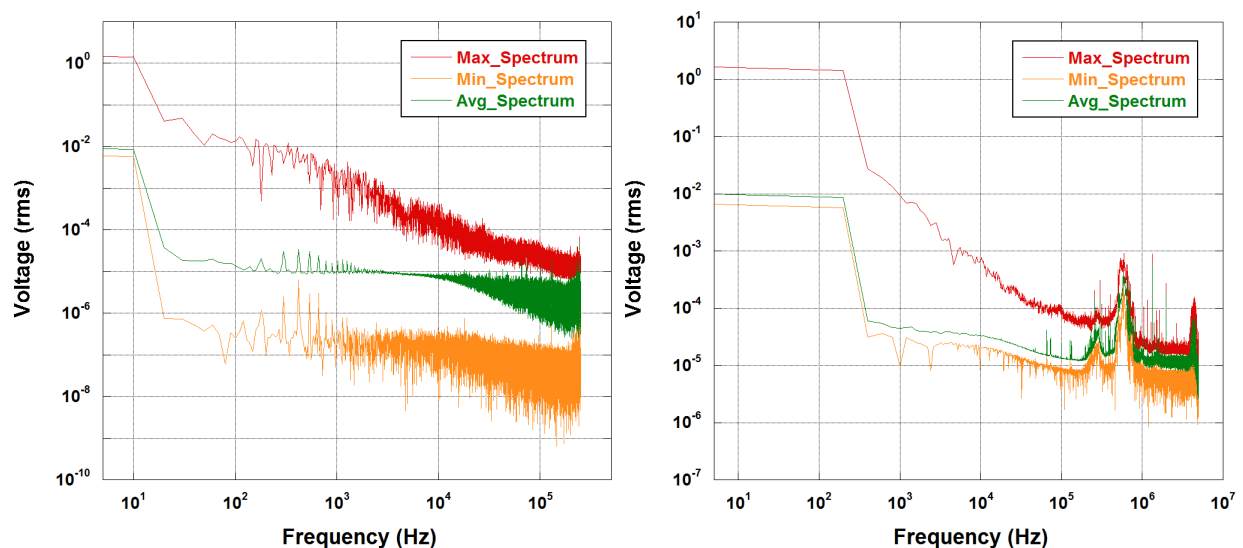


Figure 22. Maximum, minimum, and average spectral values recorded over the duration of the test. (Left) Sampled at 500 kS/s with 10 Hz resolution. (Right) Sampled at 10 MS/s with 200 Hz resolution.

The entire set of 1,999 spectra is then analyzed to obtain the maximum, minimum, and average at each frequency value. The maximum value at each frequency is recorded so that spectra containing the highest spectral components can be easily identified and retrieved for further analysis. The maximum, minimum, and average values are shown in Figure 22. The maximum curves below 200 kHz reflect a $1/f^2$ power law relationship, which is reminiscent of arcing behavior. The data also show two peaks centered

around approximately 270 kHz and 580 kHz which were not observed during the 70°C testing. As the BMU and charging equipment was not present for the 70°C test, it is possible that these spectral components are attributable to this equipment. As this spectral content is present in spectra before nail penetration, it is part of the system and not attributable to battery failure.

As Figure 22 is a composite graph capturing the maximum values from all 1,999 spectrum plots, it is desirable to identify which files captured the most significant events. This is achievable by plotting the file number for which each maximum frequency component was recorded, and then evaluate those files where the maximum values were recorded most. This is graphed in Figure 23. As can be seen, maximum values tend to be concentrated in a relatively small number of files, suggesting that relatively significant wideband events are occurring at these moments in time. Most notable are wideband events at the moment of Cell 6 failure (File 25) and during a timeframe of voltage noise, observable as drops below 0V across Cell 6 (File 678). This voltage noise is observed identically in the Cell 6 voltage data and that measured at the battery grounding terminal. As Cell 6 is no longer supplying power, this suggests power delivered from an adjacent cell (most likely from Cell 5, due to the negative bias observed across Cell 6) through Cell 6 and to the cell case. File 678 therefore records the spectral content during part of this event, specifically at the end.

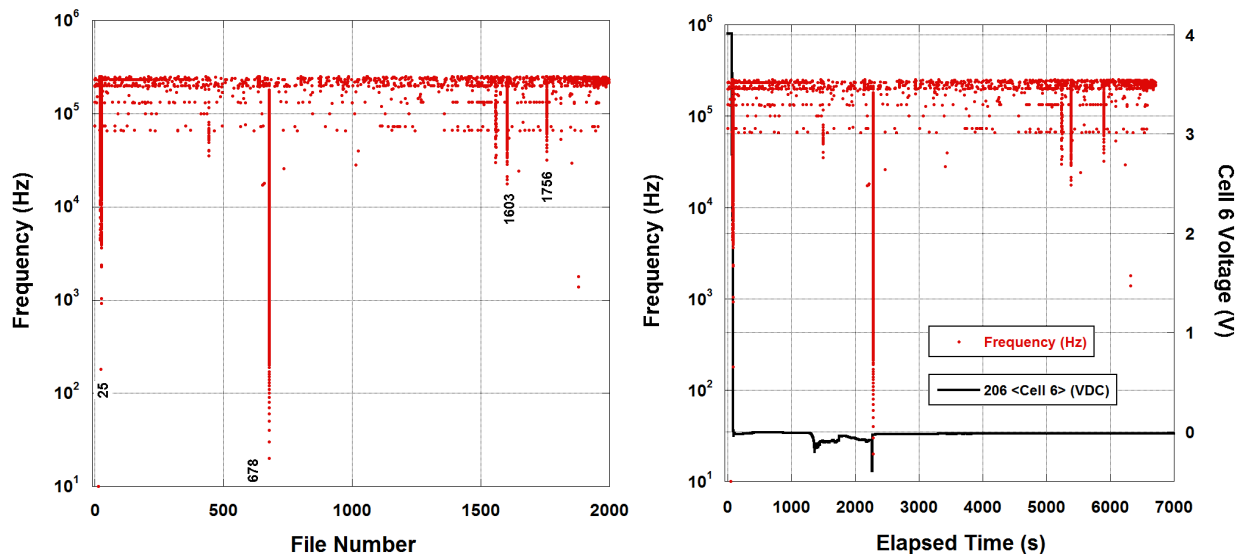


Figure 23. Location with respect to (*left*) file number and (*right*) test time of maximum amplitude for each of the 50,000 frequencies tracked in each of the 1,999 spectral files. At right the data are superimposed onto Cell 6 voltage data. Left plot lists file numbers with the most significant number of recorded maxima.

Figure 24 shows four example spectral plots from the two events containing the most significant spectral content. Figure 24 (*left*) shows the spectral content during failure of Cell 6, specifically, during the drop of



cell voltage to zero. Significant spectral content (similar in shape and magnitude to that shown for File 25) is also observed for Files 22 through 25, which spans the drop of Cell 6 voltage from 4V to zero. This spectral content does not appear to span to the failure of the ground wire. Spectral noise appears to increase by approximately one order of magnitude during the nail penetration event, possibly signifying the presence of electrical arcing. The $1/f^2$ relationship above 1 kHz is consistent with previously observed arcing behavior; the flattened response below 1 kHz does suggest presence of wideband noise, but has more of a “white noise” characteristic which has not been observed in previously observed arcing behavior. However, shorting effects as the battery interior carbonizes may be a source of this lower-frequency suppression of expected arcing magnitude.

The most significant wideband noise was observed within File 678, captured during a suspected arcing event, most likely to the battery case through Cell 6, supplied by Cell 5 and/or Cell 7. Wideband noise is observable through this discharge event, though spectral noise is most significant at the start of the event and at the end. This suggests arc strike during formation of the arcing path, and the most significant arcing event (captured in File 678) occurring at the end of the event, likely providing sufficient arc energy to destroy the arcing path, as Cell 6 and grounding voltage return to 0V at this point in time.

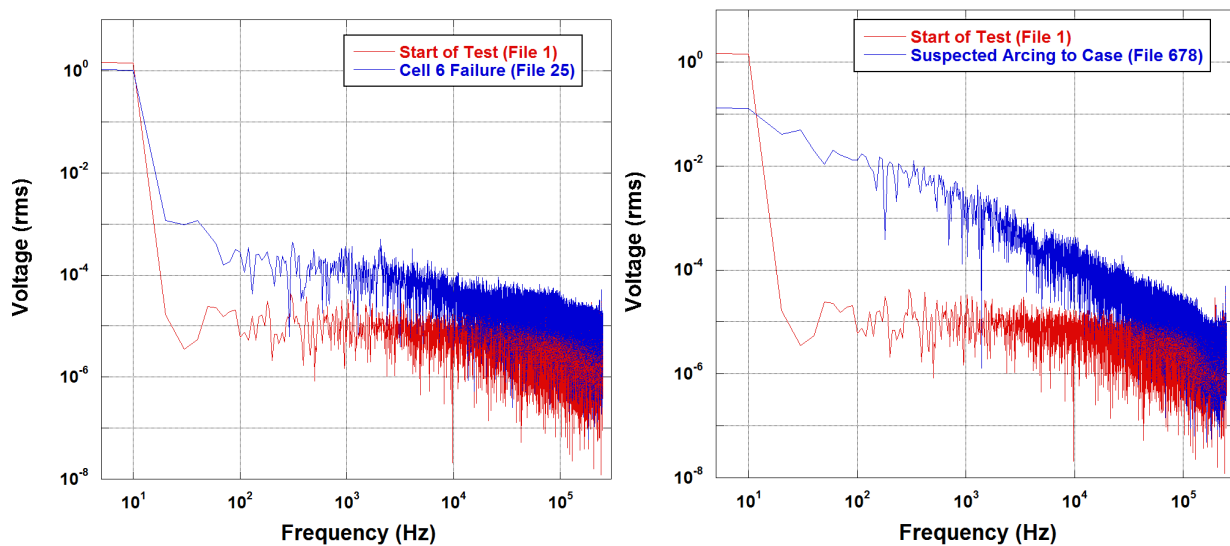


Figure 24. Spectra identified to have significant maximum frequency components. (Left) Spectrum during Cell 6 failure (File 25). (Right) Spectrum during suspected arcing to case event (File 678). Start-of-test spectrum is also shown for comparison.

The spectra can be fit to a power law relationship, which can be used to give an anticipated spectral magnitude at any given frequency. Figure 25 shows such a fit for File 678, which was recorded during the suspected arcing event to the battery case, and represented the waveform with the most spectral content



recorded during the entire test. The fit matches well between 100 Hz and 250 kHz and is consistent with electrical arcing events. This power law fit can be expressed as the following:

$$V_{rms}(f) \approx 11.0 \cdot f^{-1.07}$$

The spectrum above 250 kHz fell below the noise floor of the measurement and was subject to probable noise from the BMU and charging equipment, as well as instrument noise-related artifacts. However, prior characterization experience of electrical arcing events suggests that this $1/f^p$ power law relationship would continue to represent spectral content of arcing at higher frequencies should measurement capabilities allow for its characterization.

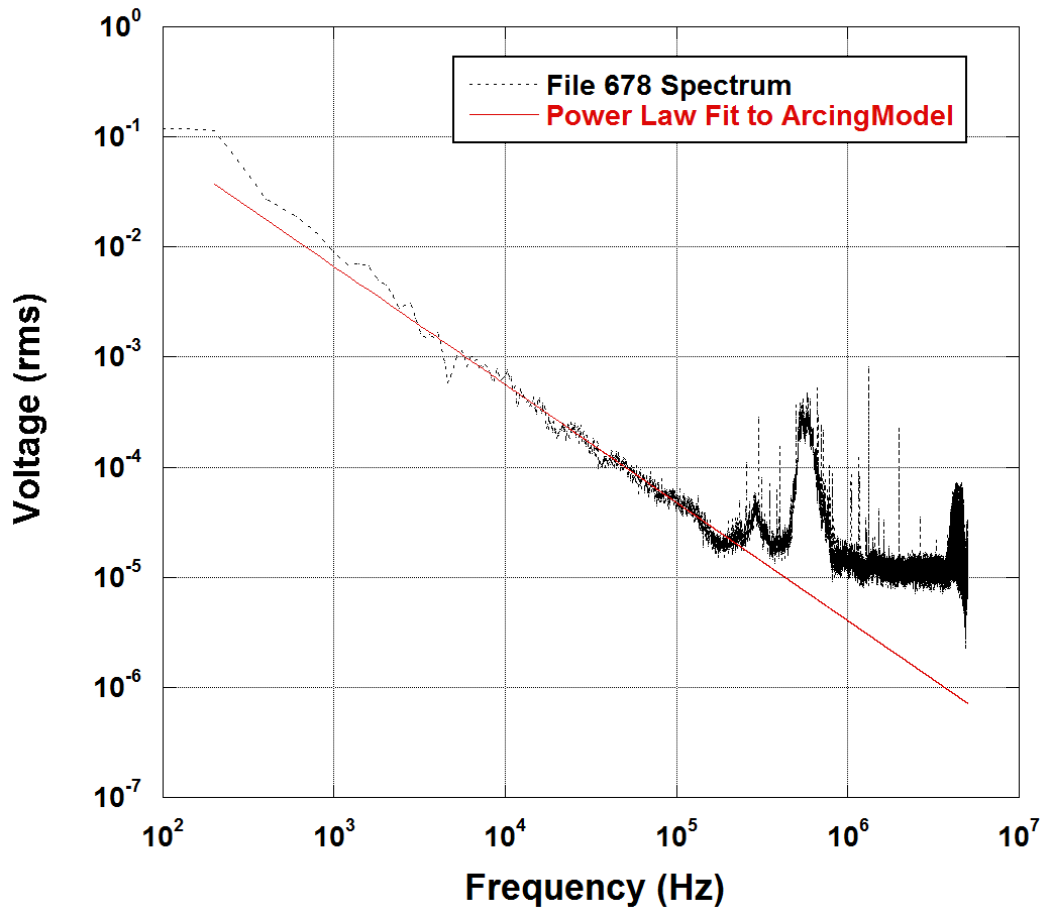


Figure 25. Power law fit to spectral data observed during suspected arcing event (File 678), showing agreement with power law fit that is consistent with electrical arcing behavior. Flattening, peaks at 270 kHz and 580 kHz, and delta artifacts above 250 kHz are result of noise floor, (likely) charging equipment, and equipment noise, respectively.



BMU Signal Outputs

The BMU signal outputs recorded during the test are shown in Figure 26 and Figure 27. The voltage outputs before and after the Cell 6 venting event are listed in Table 3. The values show that the signals are all “high”, mostly referenced near or slightly below the battery voltage at the start of the test. The signal “Battery Min SOC” goes “low” first, at the time of the first drop in cell voltage (when the first sub-cell exhibits an internal short circuit). Except for the “Battery Fail” and one of the “Inhib of Charge” signals, the rest of the signals go “low” at the onset of Cell 6 dropping to zero volts. The “Battery Fail” signal then goes “low” during the transition of Cell 6 to zero or at the moment Cell 6 reaches zero volts. The “Battery V” signal follows the battery output voltage through the first 2500 seconds of the test, with roughly a 0.4V drop from the voltage at the positive terminal of the battery.

These values attained after venting of Cell 6 hold stable until 2600 seconds into the test, where signals from the BMU become noisy and erratic (Figure 27). The exact reason for this change is not clear, but it is possible that this originates from some mechanism of electrical failure in the control circuitry inside the battery, which could be triggered from the exposure to high temperature and/or smoke contaminants from the Cell 6 venting event.

Table 3. Voltage outputs of BMU signals before and after Cell 6 venting.

BMU Signal	Before Test (V)	Time of First Transition (s)	After First Transition (V)	After Cell 6 Venting (V)
Inhib of Charge (301)	28.42	80	0.00	0.22
Inhib of Charge (302)	31.30	77	-0.09	0.62
Checksum	28.43	77	0.01	0.09
Battery Min SOC	28.43	65	-0.02	0.11
Battery V	31.76	77	28.24	27.48
Battery Fail	28.43	82	-0.02	0.64
Inhib of Charge 2	28.42	77	0.01	0.27
Checksum BMU 2	28.43	77	0.01	0.11

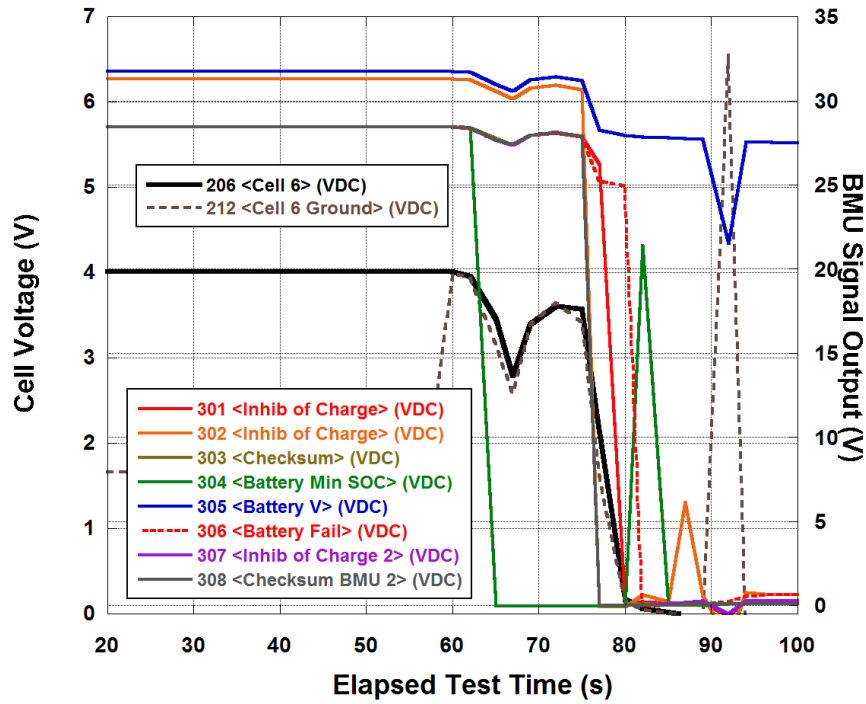


Figure 26. Signal outputs of BMU in the vicinity of venting of Cell 6.

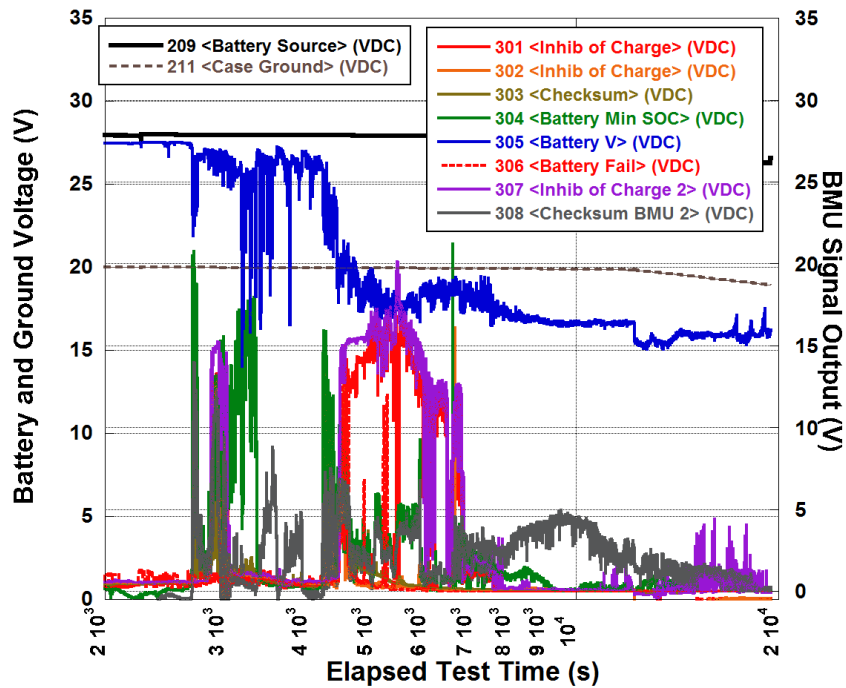


Figure 27. Signal outputs of BMU, 2000 to 10000 seconds into the test, showing erratic voltage output of BMU.



Summary of Events for 15°C Test

The battery was removed from the environmental chamber and connected to the test apparatus. Upon application of the nail, the battery internal temperature was approximately 11°C to 12°C. Approximately one minute into the test, the nail penetrated Cell 6, electrically shorting the case of Cell 6 to the positive terminal of the cell, and causing an internal short circuit within Cell 6. This caused Cell 6 to vent and release thermal energy, mostly directed towards Cells 5 and 7, though this thermal energy was not sufficient to induce venting in these adjacent cells. This venting event created a low-resistance short from the negative terminal of Cell 6 to the battery case, short circuiting Cells 1 through 5 through the 12 AWG ground wire. This pathway caused at least 600A to flow for at most three seconds, supplied by Cells 1 through 5, causing Joule heating at their respective terminals. Following fusing open of the ground wire, the battery case was biased at 20V, which was equal to the potential across Cells 1 through 5. This heating however was not sufficient to cause venting in the other cells, and raised most cell terminal temperatures to no more than 70°C. A resistive short momentarily formed across Cells 7 and 8, but this cleared rapidly and did not cause significant Joule heating on the terminals of Cells 7 and 8. After the Joule heating from the high current event began to settle, the entire battery system began to move towards thermal equilibrium, with Cells 5, 6, and 7 losing heat to the much cooler Cells 1-4 and 8. After approximately two hours the entire battery system began to lose thermal energy to the surrounding environment and began to cool. At 12,000 seconds the entire battery temperature dropped below 55°C and a 10A load was applied to the battery to remove charge from the un-vented cells. Application of this load resulted in minor heating in Cell 6, showing that Cell 6 had continuity between its terminals through a carbonized resistance in its interior.

Maximum temperatures for each thermocouple and times of occurrence are listed in Table 4.

Table 4. Maximum temperatures and corresponding time of occurrence for each thermocouple. Temperatures in bold are highest for each cell.

Table with 5 columns: Cell, Thermocouple, Max. Temp (°C), Elapsed Test Time (s), Time after Nail Penetration (m:s). Rows include data for Nail, Cell 1 (thermocouples 1101-1502), and Cell 2 (thermocouples 2101-2301).



Final Report for 787 Battery (Asset 445) Tested at 15°C, Grounded

Cell	Thermocouple	Max. Temp (°C)	Elapsed Test Time (s)	Time after Nail Penetration (m:s)
	2501	50.22	167	1:47
	2502	58.51	245	3:05
3	3101	57.60	4915	80:55
	3201	51.90	4682	77:02
	3301	55.31	3952	64:52
	3501	53.84	5792	95:32
	3502	59.31	2557	41:37
4	4101	49.24	6130	101:10
	4201	48.22	6665	110:05
	4301	55.44	6142	101:22
	4501	52.86	6675	110:15
	4502	66.89	3810	62:30
5	5101	216.2	947	14:47
	5201	72.68	3145	51:25
	5301	84.16	3052	49:52
	5501	199.5	745	11:25
	5502	339.9	322	4:22
6	6101	342.5	87	0:27
	6201	300.7	555	8:15
	6301	277.9	455	6:35
	6501	330.5	482	7:02
	6502	71.00	4085	67:05
7	7101	86.14	1260	20:00
	7201	180.4	1050	16:30
	7301	141.5	732	11:12
	7501	69.35	3149	51:29
	7502	52.54	89	0:29
8	8101	48.07	5137	84:37
	8201	58.91	3714	60:54
	8301	54.64	6430	106:10
	8501	47.77	6755	111:35
	8502	56.76	4687	77:07

Post Test Disassembly

The battery was disassembled after discharging the cells. The photographic documentation of the disassembled battery is presented in Appendix A. Figure 28 shows the potential locations of each melted/open collector within each cell. For this test, no such melting/opening was observed.

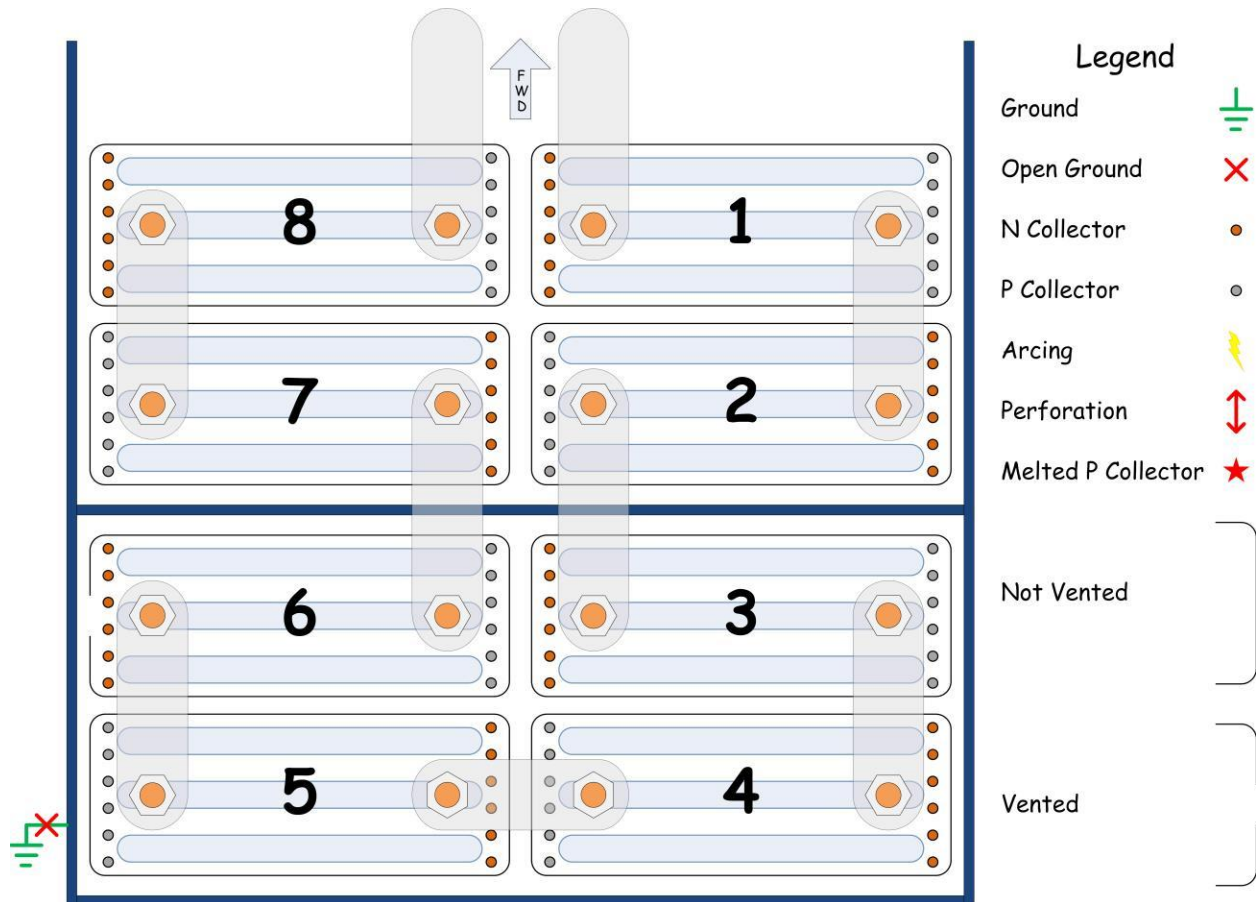


Figure 28. Locations of melted/open collectors inside each battery cell.

The pattern of failure from other tests suggests the failure mechanism as shown in Figure 29, and the corresponding voltage behavior is shown in Figure 30. In this model, heat transferred to the cell (e.g., from a previously vented cell) causes one of the three sub-cells to short circuit and draw large current from the rest of the cell. This causes the aluminum electrodes to overheat and open on the cell which is in a short-circuit condition. During short-circuit the voltage of the cell drops, but then recovers once the

shorted cell is removed from the circuit. The heat from the failed sub-cell then transfers to the other two sub-cells, causing thermal runaway for the rest of the cell and drop of the cell voltage to zero. This failure model suggests that the electrodes that fused open will denote the sub-cell which failed first, and is expected to help in determining the sequence of cell failure by signaling the direction of heat flow into the cell which caused failure. This also suggests that open electrodes at the center sub-cell suggests that heating originated from within the cell rather than from an adjacent cell, increasing the probability that the cell showing open electrodes at the center sub-cell only was the cell that was first to fail and triggered the entire failure event.

Since no propagation of cell venting was observed in this test, nor were any electrodes observed to have failed open, the results were not able to be used to correlate this proposed failure mechanism.

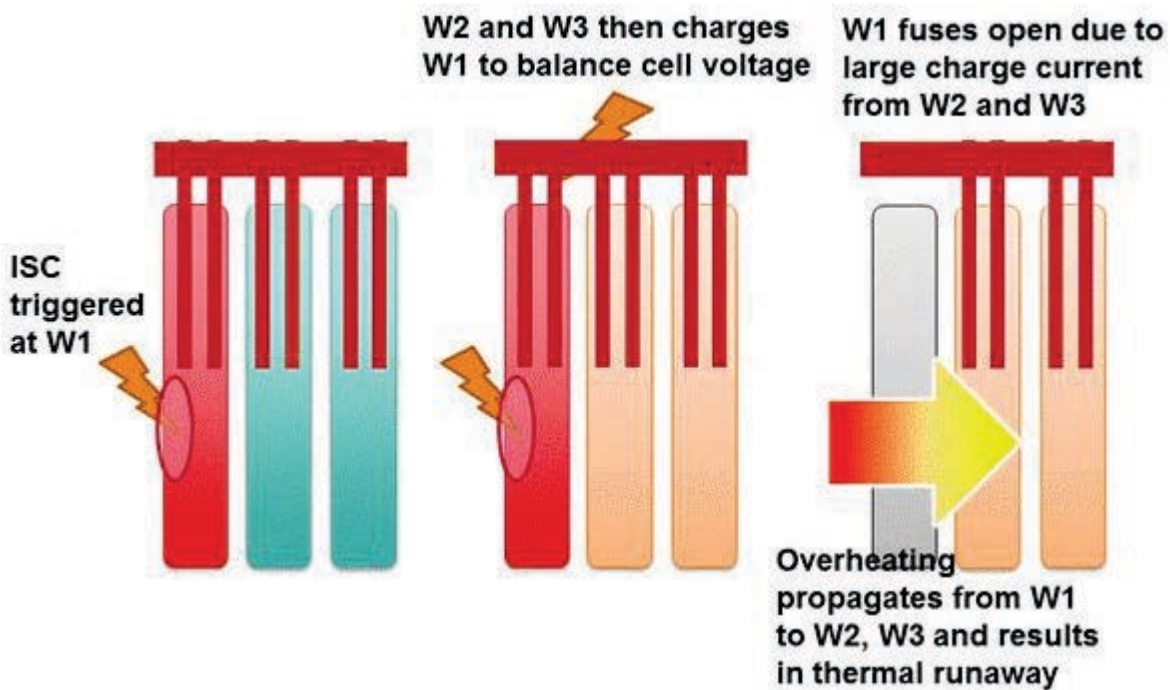


Figure 29. Proposed failure mechanism for cells.

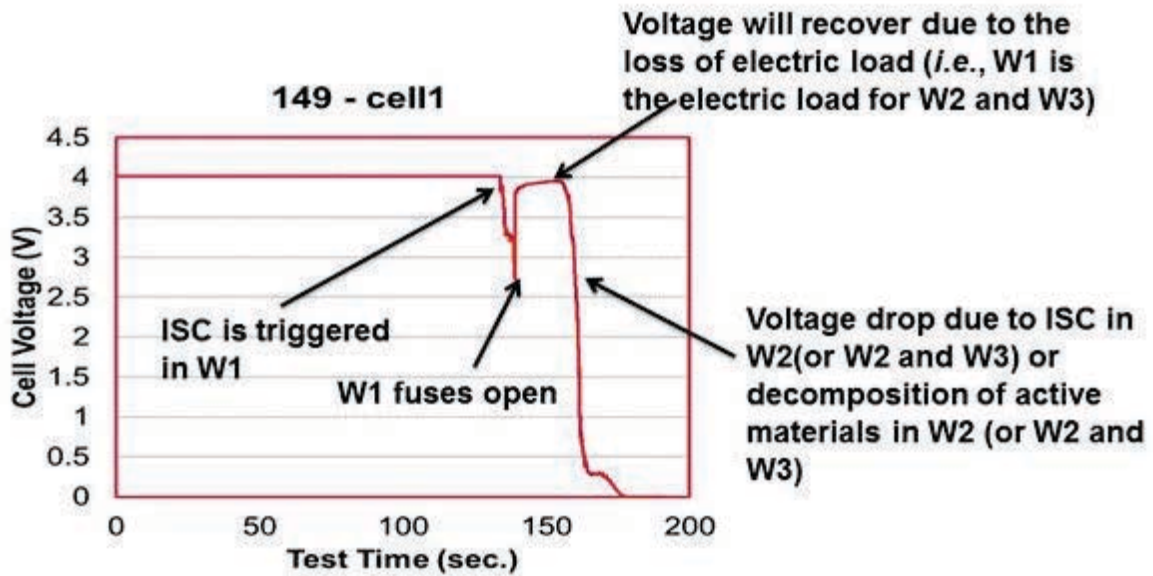


Figure 30. Cell voltage behavior during failure mechanism as shown in Figure 29.



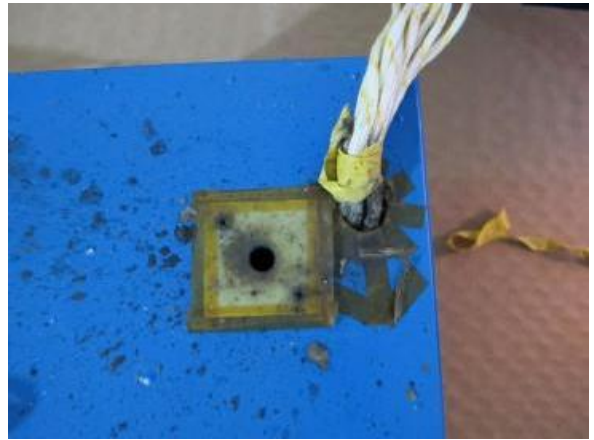
APPENDIX A – POST-TEST DISASSEMBLY PHOTOS

Post- Test Photos – Nail Penetration Apparatus and Intact Battery



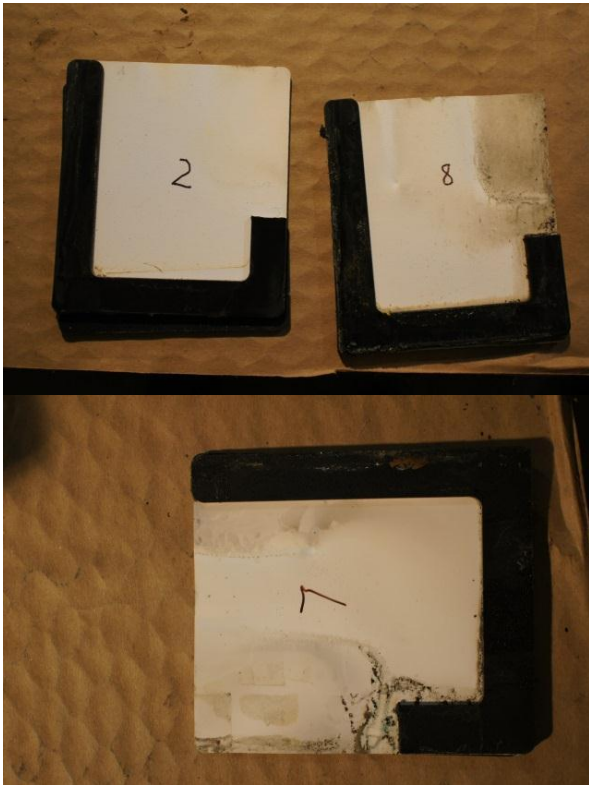
Post Test Disassembly Photos – Intact Battery





Battery Post Test Disassembly Photos - Insulation Materials

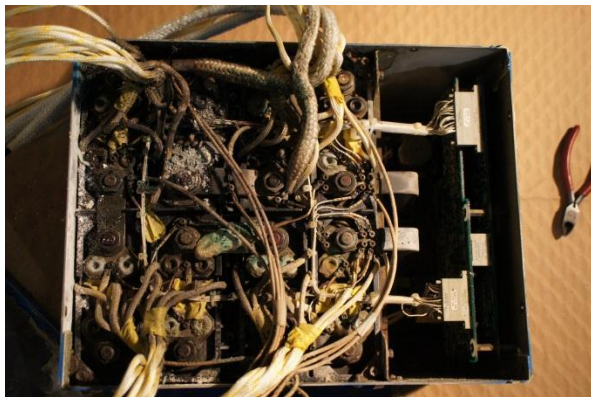
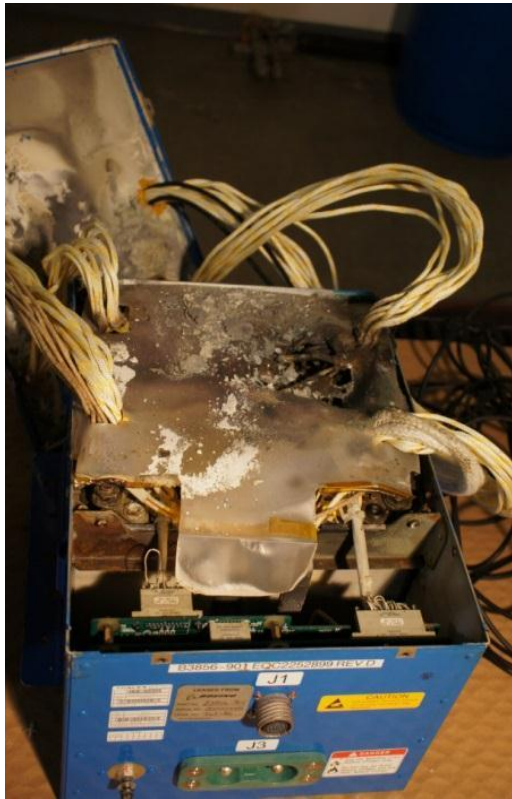


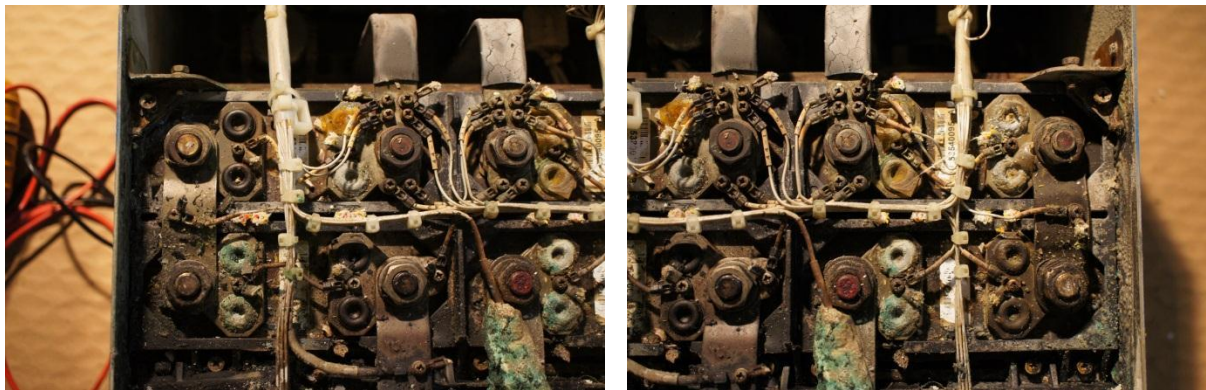






Intact Battery Post Test Disassembly Photos – Top of Battery











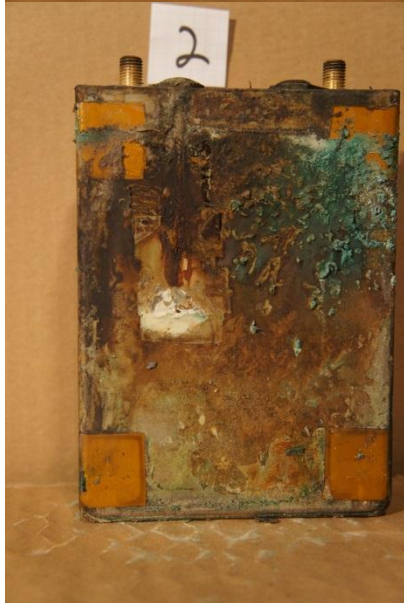
Battery Post Test Disassembly Photos – Cell 1







Battery Post Test Disassembly Photos – Cell 2







Battery Post Test Disassembly Photos – Cell 3



Battery Post Test Disassembly Photos – Cell 4



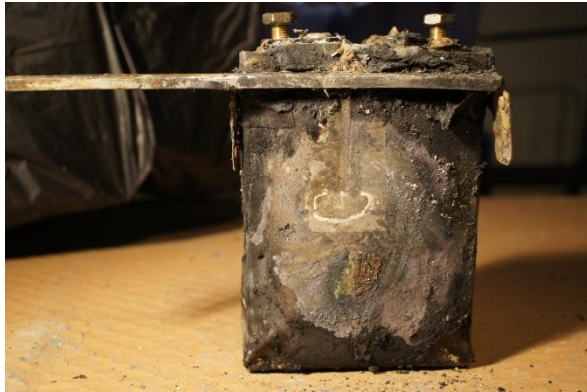


Battery Post Test Disassembly Photos – Cell 5





Battery Post Test Disassembly Photos – Cell 6



















Battery Post Test Disassembly Photos – Cell 7





Battery Post Test Disassembly Photos – Cell 8







APPENDIX B – BATTERY PRE-TEST DISASSEMBLY ANALYSIS

- Battery Part Number: B3856-901
- Battery Serial Number: 445
- Ambient Temperature at Examination: 75.92°F
- Humidity at Examination: 56%
- Start Time: 10:50
- Stop Time: 11:50
- Total Time: 1 hr

Internal Battery Disassembly



Caution: Electrostatic Discharge Sensitive protection is required.
WARNING! Full battery voltage potential is present!
Personal protective equipment is required.

Remove the cover. Take picture of internal battery and record photo # 445_0994.
Tape the edge of box before start. Number the cells and bus bars in a clockwise direction.

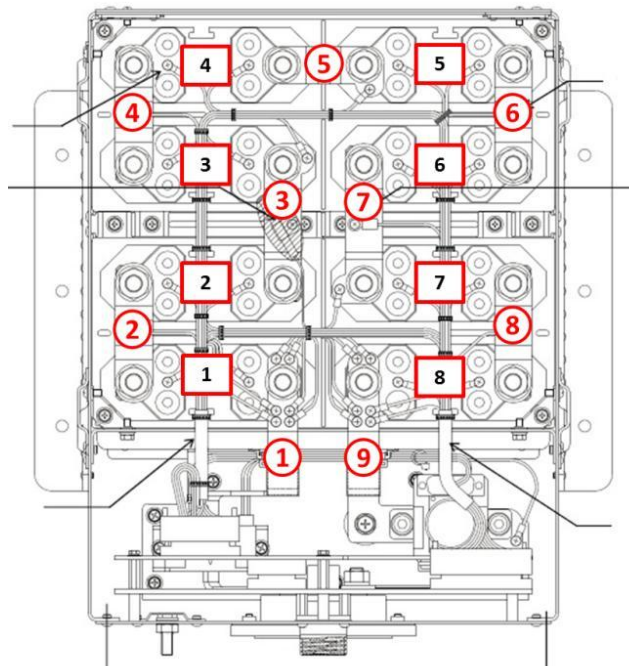


Figure 31. Numbering of the cells and bus bar



Remove the screw of wire “33-A”, “43-I” and “39-F”; put the wire in plastic sleeves.

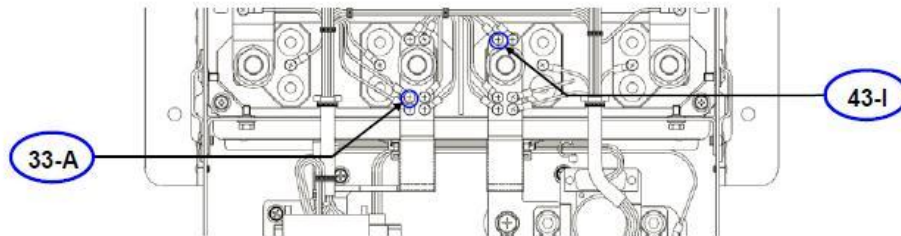


Figure 32. Terminal positions “No. 43-I” and “No. 33-A” of Sub Harness

Put a sheet on cell and disconnect the Sub Harness (210), then disconnect the Main Harness (160). Cut the cable tie and tape the harness on the outside of box.

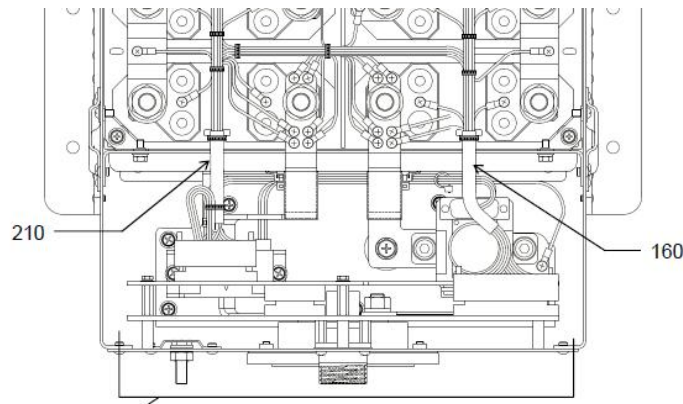


Figure 33. Positions of Sub Harness (210) and Main Harness (160)

Disconnect the HECS contactor harness (360) with wood stick.

Remove the screw of wire “38-E” and put sleeve.

Loosen the nuts on bus bar No. 5 and remove it, put sleeve on terminals.

Unscrew the screws on four corners in the outside box to avoid arcing.

Remove the screws on each bus bar and put sleeve on No. 7.

Unscrew the nuts of each bus bar and remove bars, put sleeve on terminals.

Visual observation of bus bar after removing it, take photo if anything unusual.



Bus Bar Observation

IPL #	IPL Nomenclature	Inspection Results	Photo #s
	Bus bar 2	Unremarkable	
	Bus bar 3	Unremarkable	
	Bus bar 4	Unremarkable	
	Bus bar 5	Unremarkable	
	Bus bar 6	Unremarkable	
	Bus bar 7	Unremarkable	
	Bus bar 8	Unremarkable	

Unscrew all screws on each cell and cut cable tie, then remove the whole wire.

Loosen nuts of Positive and Negative bar, bending the bars toward ████ side and put sleeve on terminals.

Unscrew and remove the corner metal fitting.

Unscrew and remove the fixation frame above cells.

Measure OCV.

Equipment Documentation

Equipment	Model	Property Number	Calibration Date
TRUE RMA MULTIMETER	Fluke 289	21120134	2013-09-23



OCV Measurement

Cell #	Results			
	V1 (V)	V2 (V)	V1-V2 (mV)	V1-V2>20mV (Y/N?)
1	3.7028	3.7024	0.4	N
2	3.7047	3.7044	0.3	N
3	3.7034	3.7032	0.2	N
4	3.7958	3.7055	0.3	N
5	3.7032	3.7030	0.2	N
6	3.7053	3.7051	0.2	N
7	3.7033	3.7031	0.2	N
8	3.7056	3.7053	0.3	N

Take cell and insulation plates and spacers out. Visual observation and record any unusual phenomena.

Cell Observations

IPL #	IPL Nomenclature	Inspection Results	Photo #s
	Cell 1	Unremarkable	
	Cell 2	Unremarkable	
	Cell 3	Unremarkable	
	Cell 4	Unremarkable	
	Cell 5	Unremarkable	
	Cell 6	Unremarkable	
	Cell 7	Unremarkable	
	Cell 8	Unremarkable	

Measure and record the dimension and weight of each cell.



Equipment Documentation

Equipment	Model	Property Number	Calibration Date
Vernier Caliper	Mitutoyo CD-6" CSX	CAS 413	2013-02-26

Cell Dimension and Weight Measurement

Battery S/N	Cell #	Cell S/N	Weight (g)	Dimension (mm)
445	1	53800088 A	NA	D(+)Up.: 51.28
				D(+)Mid.: 50.87
				D(+)Lo.: 50.25
				D(-)Up.: 51.06
				D(-)Mid.: 50.89
				D(-)Lo.: 50.22
				L Up.: 132.91
				L Mid.: 133.08
				L Lo.: 131.58
				H(+):176
				H(-): 176



Final Report for 787 Battery (Asset 445) Tested at 15°C, Grounded

Battery S/N	Cell #	Cell S/N	Weight (g)	Dimension (mm)
445	2	53800112 B	NA	D(+)Up.: 50.88
				D(+)Mid.: 50.90
				D(+)Lo.: 50.22
				D(-)Up.: 51.06
				D(-)Mid.: 50.77
				D(-)Lo.: 50.26
				L Up.: 132.82
				L Mid.: 133.12
				L Lo.: 132.34
				H(+): 176
				H(-): 176
Battery S/N	Cell #	Cell S/N	Weight (g)	Dimension (mm)
445	3	53800093 A	NA	D(+)Up.: 51.14
				D(+)Mid.: 50.76
				D(+)Lo.: 50.02
				D(-)Up.: 51.04
				D(-)Mid.: 50.81
				D(-)Lo.: 50.09
				L Up.: 133.04
				L Mid.: 133.13
				L Lo.: 131.72



Final Report for 787 Battery (Asset 445) Tested at 15°C, Grounded

				H(+): 176
				H(-): 176
Battery S/N	Cell #	Cell S/N	Weight (g)	Dimension (mm)
445	4	53800116 B	NA	D(+)Up.: 50.96
				D(+)Mid.: 50.75
				D(+)Lo.: 50.05
				D(-)Up.: 50.84
				D(-)Mid.: 50.93
				D(-)Lo.: 50.06
				L Up.: 132.91
				L Mid.: 132.98
				L Lo.: 131.81
				H(+): 176
H(-): 176				
Battery S/N	Cell #	Cell S/N	Weight (g)	Dimension (mm)
445	5	53800096 A	NA	D(+)Up.: 50.97
				D(+)Mid.: 50.78
				D(+)Lo.: 50.05
				D(-)Up.: 51.00
				D(-)Mid.: 50.84
				D(-)Lo.: 50.07
				L Up.: 133.16



Final Report for 787 Battery (Asset 445) Tested at 15°C, Grounded

				L Mid.: 133.06
				L Lo.: 131.87
				H(+): 176
				H(-): 176
Battery S/N	Cell #	Cell S/N	Weight (g)	Dimension (mm)
445	6	53800186 B	NA	D(+)Up.: 51.24
				D(+)Mid.: 50.94
				D(+)Lo.: 50.14
				D(-)Up.: 51.00
				D(-)Mid.: 50.96
				D(-)Lo.: 50.12
				L Up.: 132.81
				L Mid.: 132.68
				L Lo.: 131.86
				H(+): 176
				H(-): 176
Battery S/N	Cell #	Cell S/N	Weight (g)	Dimension (mm)
445	7	53800139 A	NA	D(+)Up.: 51.07
				D(+)Mid.: 50.97
				D(+)Lo.: 50.10
				D(-)Up.: 51.14
				D(-)Mid.: 50.91



Final Report for 787 Battery (Asset 445) Tested at 15°C, Grounded

Battery S/N	Cell #	Cell S/N	Weight (g)	Dimension (mm)
445	8	53800193 B	NA	D(-)Lo.: 50.09
				L Up.: 133.29
				L Mid.: 132.93
				L Lo.: 131.85
				H(+): 176
				H(-): 176
				D(+)Up.: 51.06
				D(+)Mid.: 50.98
				D(+)Lo.: 50.23
				D(-)Up.: 51.05
				D(-)Mid.: 50.91
				D(-)Lo.: 50.12
				L Up.: 132.88
L Mid.: 133.14				
L Lo.: 131.88				
H(+): 176				
H(-): 176				

APPENDIX C – INFRARED SPECTRA FROM ASSET 445 NAIL PENETRATION TEST

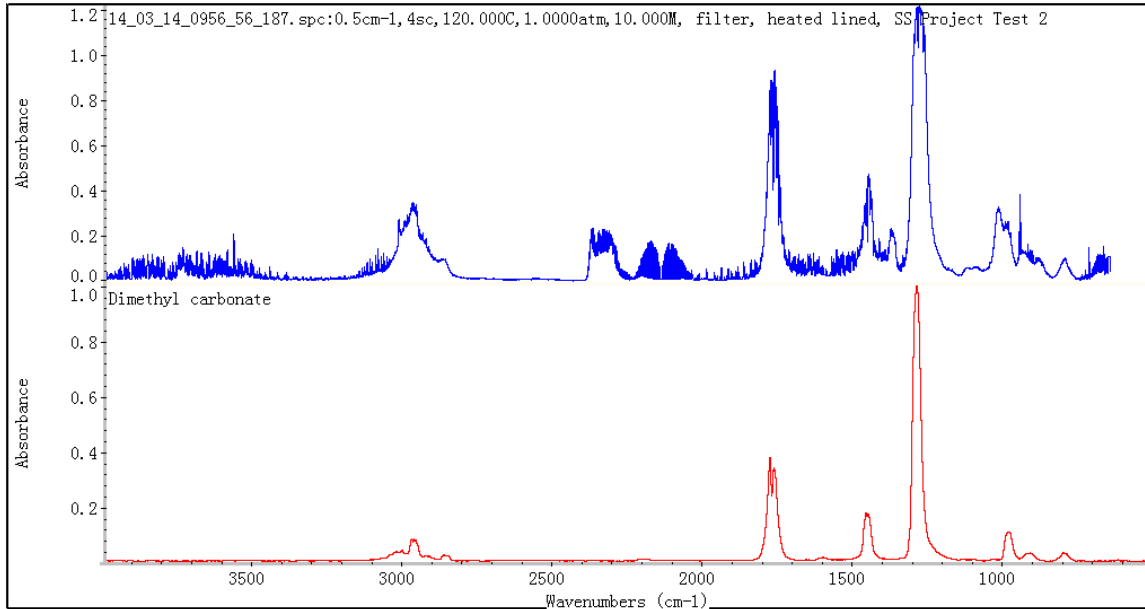


Figure 34. Spectrum of zone A compare to standard spectrum of Dimethyl Carbonate; DMC.

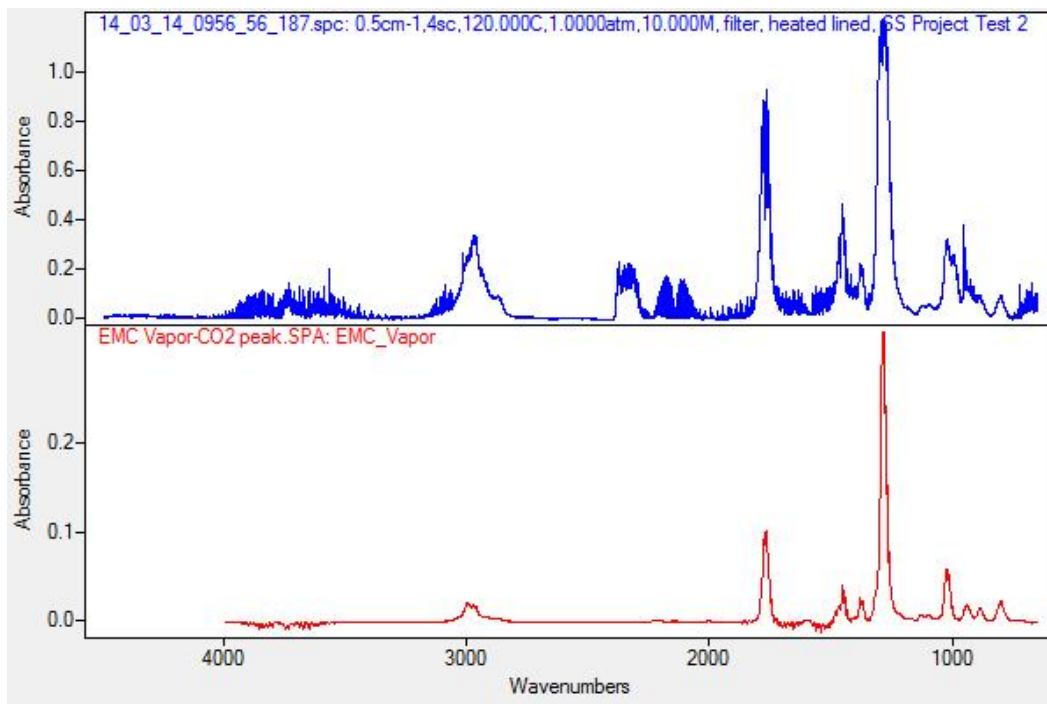


Figure 35. Spectrum of zone A compare to standard spectrum of Ethylmethyl Carbonate; EMC

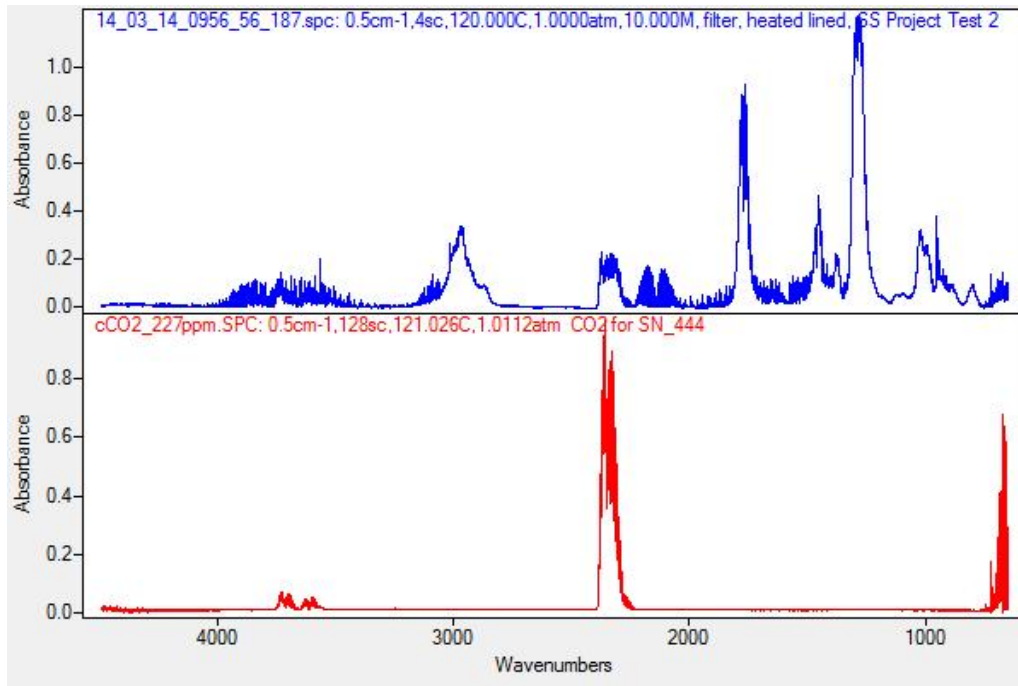


Figure 36. Spectrum of zone A compare to standard spectrum of Carbon dioxide; CO₂.

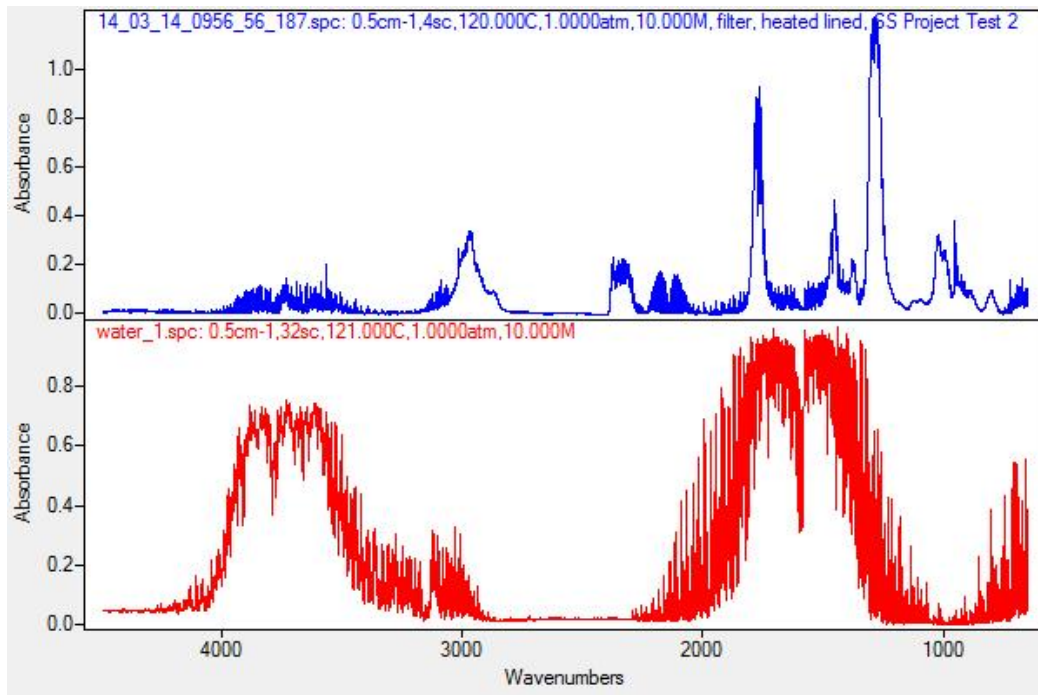


Figure 37. Spectrum of zone A compare to standard spectrum of Water; H₂O.

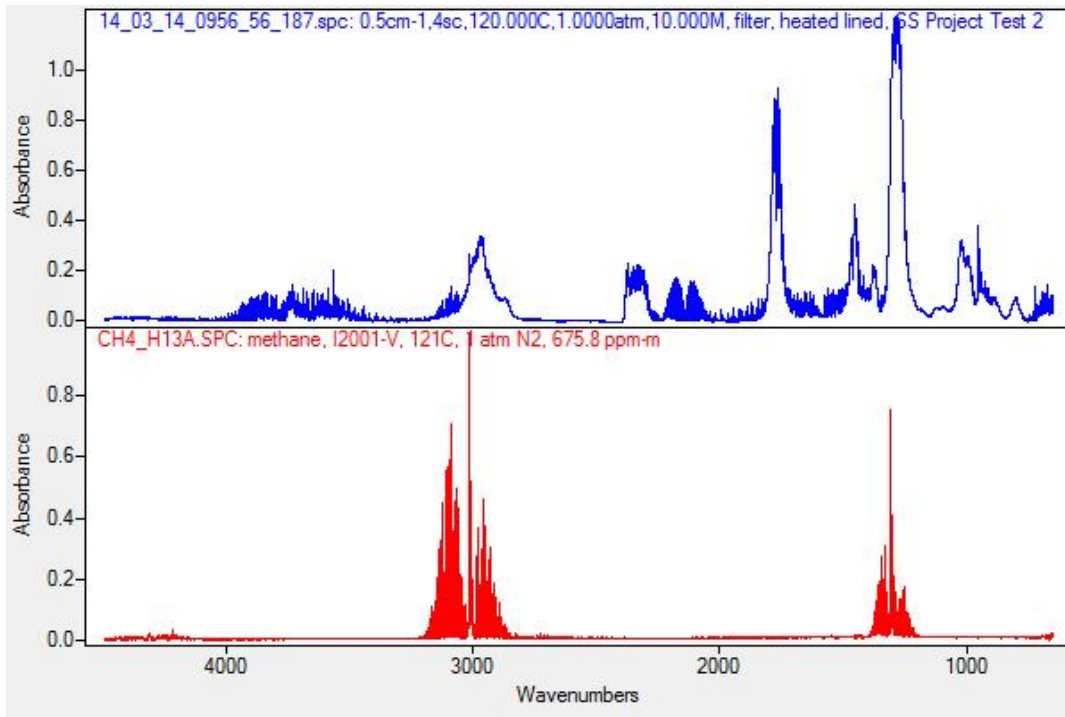


Figure 38. Spectrum of zone A compare to standard spectrum of Methane; CH₄.

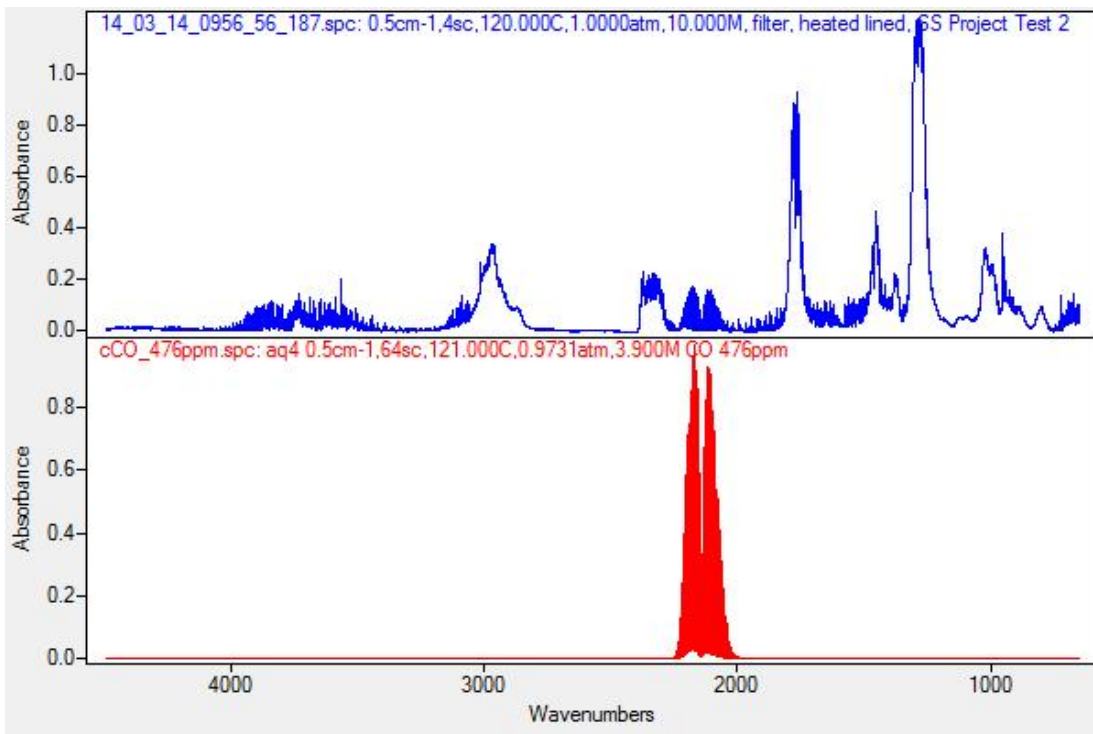


Figure 39. Spectrum of zone A compare to standard spectrum of Carbon monoxide; CO.

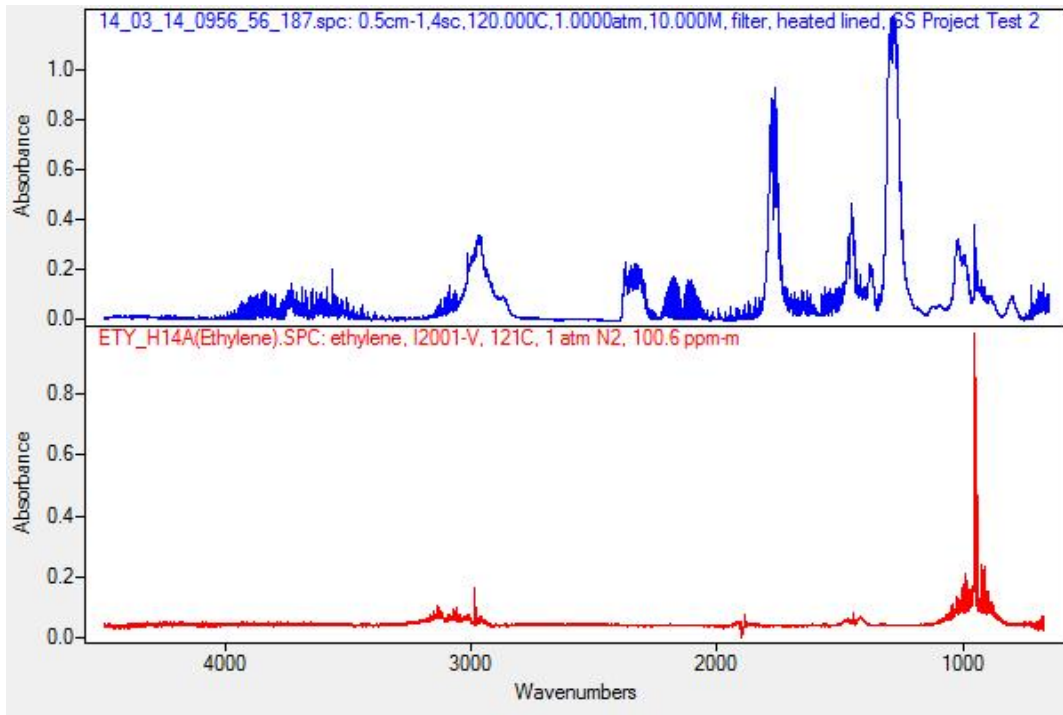


Figure 40. Spectrum of zone A compare to standard spectrum of Ethylene, C₂H₄.

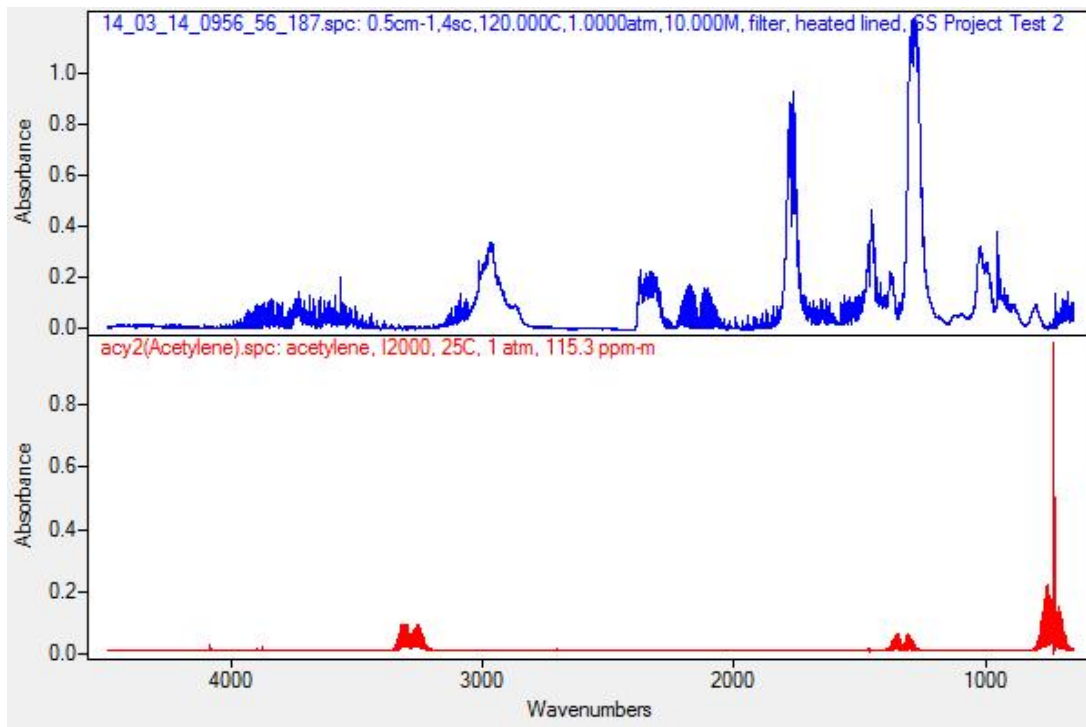


Figure 41. Spectrum of zone A compare to standard spectrum of Acetylene, C₂H₂.